ISO spectroscopy of gas and dust: from molecular clouds to protoplanetary disks

Dishoeck, E.F. van

Citation

Dishoeck, E. F. van. (2004). ISO spectroscopy of gas and dust: from molecular clouds to protoplanetary disks. Retrieved from https://hdl.handle.net/1887/2206

Annu. Rev. Astron. Astrophys. 2004. 42:119–67
doi: 10.1146/annurev.astro.42.053102.134010

ISO SPECTROSCOPY OF GAS AND DUST: From Molecular Clouds to Protoplanetary Disks

Ewine F. van Dishoeck
Leiden Observatory, PO Box 9513, 2300 RA Leiden, The Netherlands;
email: ewine@strw.leidenuniv.nl

Key Words infrared: spectroscopy, star formation, interstellar molecules, interstellar dust, circumstellar matter

■ **Abstract** Observations of interstellar gas-phase and solid-state species in the 2.4–200 μm range obtained with the spectrometers on board the *Infrared Space Observatory* (*ISO*) are reviewed. Lines and bands caused by ices, polycyclic aromatic hydrocarbons, silicates, and gas-phase atoms and molecules (in particular H_2, CO, H_2O, OH, and CO_2) are summarized and their diagnostic capabilities illustrated. The results are discussed in the context of the physical and chemical evolution of star-forming regions, including photon-dominated regions, shocks, protostellar envelopes, and disks around young stars.

1. INTRODUCTION

During the formation of stars deep inside molecular clouds, the surrounding gas and dust become part of the infalling envelope feeding the central object. The protostars themselves are extinguished by hundreds of magnitudes, so that the circumstellar gas and dust are the only tracers of the physical processes happening inside. A study of the characteristics of the circumstellar gas and dust is therefore key to understanding the origin of stars. Part of this gas and dust ends up in the rotating disks surrounding young stars, and forms the basic material from which icy planetesimals, and ultimately rocky and gaseous planets, are formed. Spectroscopic surveys of star-forming regions at different evolutionary stages, therefore, also provide quantitative information on the building blocks available during planet formation. The *Infrared Space Observatory* (*ISO*)[1] has provided

---

[1] *ISO* was a project of the European Space Agency (ESA) with instruments funded by ESA member states (especially the PI countries: France, Germany, The Netherlands, and the United Kingdom) and with the participation of the Institute of Space and Astronautical Science of Japan (ISAS) and the National Aeronautics and Space Administration (NASA) (Kessler et al. 1996, 2003).

the first opportunity to obtain complete infrared (IR) spectra from 2.4–200 μm unhindered by the Earth's atmosphere.

At the temperatures characteristic of star-forming regions, most of the radiation emerges at mid- and far-IR wavelengths, the majority of which is blocked from Earth. Most young stellar objects (YSOs) have been found through ground-based IR surveys and the *Infrared Astronomical Satellite* (*IRAS*). The spectra of the coldest protostellar objects (ages of $\sim 10^4$ years since collapse began) peak around 100 μm and such sources are best studied with ground-based submillimeter telescopes and the longest wavelength instruments on *ISO*. Once the dense envelopes start to dissipate owing to the effects of outflows, the objects become detectable at mid-IR wavelengths, around ages of $\sim 10^5$ years, and are accessible to the shorter wavelength instruments on *ISO*. The outflows also create shocks in the surrounding molecular cloud, which emit brightly in mid-IR lines. If ultraviolet (UV) radiation from the young stars can escape, it heats the neighboring gas and photodissociates molecules, creating so-called photon-dominated or photodissociation regions (PDRs). The tremendous range in physical conditions in these different phases, with densities from 10^4 to 10^{13} cm^{-3} and temperatures from 10 to 10,000 K, are reflected in the abundances and excitation of the atoms and molecules. The *ISO* spectroscopic data therefore contain a wealth of information with which to unravel the physical and chemical processes during star and planet formation.

ISO's main contributions have been in the following areas. First, the complete wavelength coverage has provided an unbiased overview of the major gas- and solid-state species in star-forming regions, including an inventory of the reservoirs of the major elements (C, O, N, ...). Indeed, the identifications of many species have become much more secure because of the broad spectral range without gaps owing to Earth's atmosphere. Second, *ISO* was particularly well suited to study the physical structure of warm gas in the important 100–2000 K regime, which is difficult to probe with ground-based telescopes: Submillimeter CO line observations trace cold ($<$100 K) gas, whereas near-IR H_2 and optical atomic lines refer to much hotter ($\geq$2000 K) gas. Third, *ISO* has quantified the energetics of star-forming regions, by measuring directly the photoelectric heating efficiency as well as the total cooling power in all relevant lines. Finally, the sensitivity of the instruments has allowed much larger samples to be probed so that systematic trends and characteristics at each stage of evolution could be determined. Much of this progress would not have been possible without dedicated laboratory astrophysics and theoretical chemistry studies to provide the basic molecular and solid-state data needed to analyze the *ISO* spectra.

This review summarizes the spectroscopic results from all four *ISO* instruments (see Table 1 for characteristics). The bulk of the data come from the Short Wavelength Spectrometer (SWS) and Long Wavelength Spectrometer (LWS), but relevant spectra obtained with the Camera-Circular Variable Filter (CAM-CVF) and Photometer-Spectrometer (PHOT-S) are included. It is heavily biased toward *ISO* results only, but the science case builds on pioneering observations performed prior to *ISO* with ground-based and airborne IR telescopes, in particular the *Kuiper*

TABLE 1 Spectrometers on the *Infrared Space Observatory*

Instrument	Wavelength range (μm)	Resolving power ($\lambda/\Delta\lambda$)	Aperture (arcsec)	References
SWS	2.4–45.2	1500[a]	14 × 20 – 20 × 33	de Graauw et al. 1996a
	11.4–44.5	30000	10 × 39 – 17 × 40	
LWS	43–197	200	$\sim$80[b]	Clegg et al. 1996
		10000	$\sim$80[b]	
CAM-CVF	2.3–16.5	35–50	12 × 12	Cesarsky et al. 1996
PHOT-S	2.5–5, 5.8–11.6	90	24 × 24	Lemke et al. 1996

[a] Varying with wavelength from 1000 to 2500; full spectral scans have usually been obtained with a factor-of-2 lower spectral resolution.

[b] Diameter of circular aperture.

Airborne Observatory (*KAO*) (Haas et al. 1995), and with the *IRAS* and the *Infrared Telescope in Space* (*IRTS*) missions. A historical review of those data in the context of the *ISO* results has been given by van Dishoeck & Tielens (2001). Also, more recent results from complementary ground-based facilities and new scientifically related space missions such as the *Submillimeter Wave Astronomical Satellite* (*SWAS*) and the *ODIN Satellite* are mentioned only in passing.

Owing to space limitations, this review focuses on spectroscopy of galactic molecular clouds and the immediate surroundings of YSOs.[2] Figures 1–3 illustrate the striking variety of spectral features associated with active star-forming regions. *ISO* imaging has also contributed to our understanding of the interstellar medium, especially through spatial variations in grain components (e.g., Abergel et al. 2002), the discovery of IR dark clouds (Bacmann et al. 2000, Omont et al. 2003) and studies of the coldest pre-stellar cores (Ward-Thompson et al. 2002, Krause et al. 2003), but details are not covered here. This review also does not include ionized regions of the interstellar medium, nor the circumstellar material around evolved post-AGB stars and planetary nebulae (Molster & Waters 2003). A general overview of interstellar dust has been given by Draine (2003), whereas extragalactic *ISO* spectra have been summarized by Genzel & Cesarsky (2000). Even with these limitations, it is not possible to refer to all *ISO* spectroscopy results. Many of them have been summarized in dedicated *ISO* conferences, including Heras et al. (1997), Yun & Liseau (1998), Waters et al. (1998), Cox & Kessler (1999), d'Hendecourt et al. (1999), and Salama et al. (2000).

---

[2] Protostar refers strictly to objects that derive most of their luminosity from accretion and have $L_{submm}/L_{bol} > 0.5\%$ and $M_{env}/M_* > 1$ (André et al. 2000). Young stellar object refers to all embedded stages of star formation and associated phenomena such as outflows. In this review, the term protostar is used loosely to also refer to the more evolved embedded stages, especially in the context of high-mass objects.

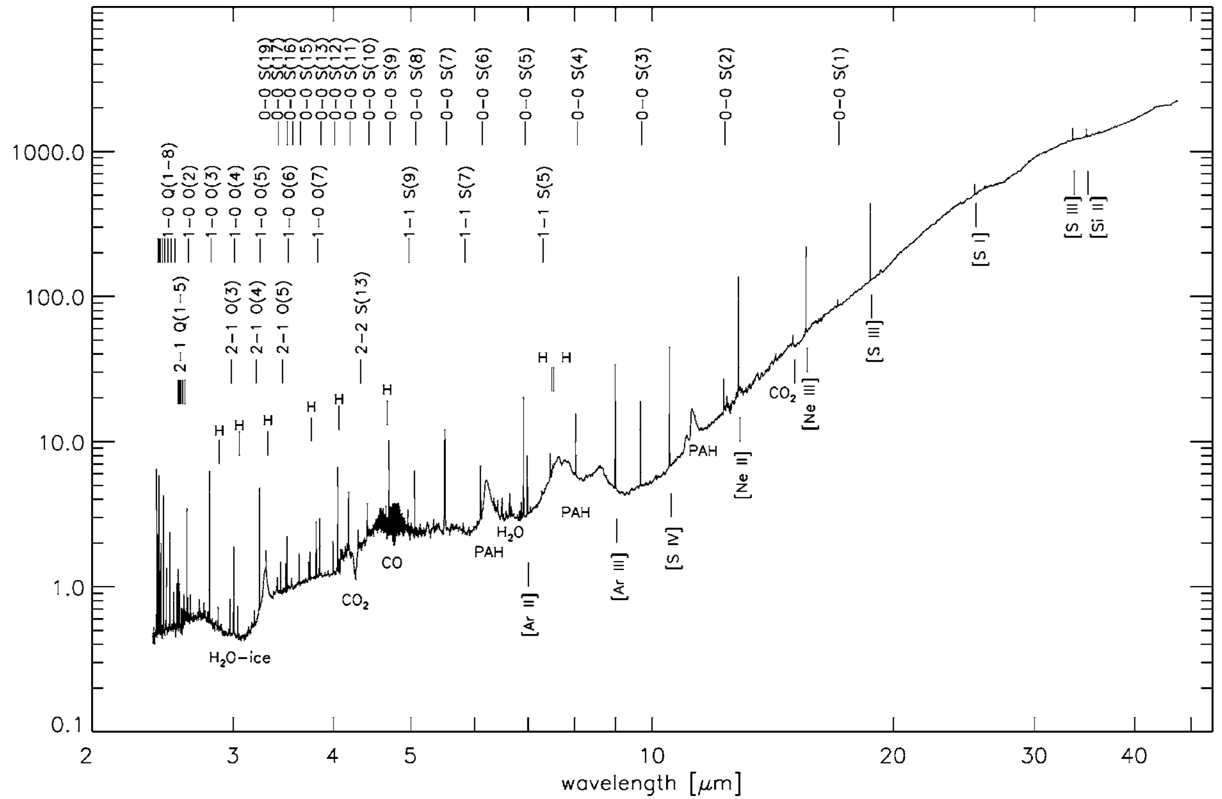

Figure 3 SWS grating scan of the Orion Peak 1 shock, showing a rich forest of H_2 lines and other features (Rosenthal et al. 2000).

2. INFRARED SPECTROSCOPIC FEATURES

The mid- and far-IR wavelength ranges are spectacularly rich in spectral features, many of which probe unique species that cannot be observed at any other wavelength. The wealth of sharp gas-phase lines and broad solid-state bands is illustrated in the SWS spectrum of one of the brightest mid-IR sources in the sky, the Orion-KL region (Figure 3). Each of these features (summarized in Table 2) has its own diagnostic capability.

2.1. Atomic Lines

Fine-structure transitions within the lowest electronic term of most astrophysically relevant atoms and ions occur at mid-IR wavelengths. Many of them are found in H II regions where they are used to probe the hardness of the radiation field, but some lines are observed in the neutral clouds discussed here, e.g., [S I] 25.2, [Si II] 34.8, [O I] 63.2 and 145.5, and [C II] 157.7 μm.[3] These are key diagnostics of photon- versus shock-heating. H I recombination lines are often seen in mid-IR spectra of ionized gas, but not in those of neutral clouds.

2.2. H_2 and HD Pure Rotational Lines

The lowest transitions of the most abundant molecule in the universe, H_2, occur at mid-IR wavelengths, and probe directly the bulk of the warm gas and its temperature. Most of the deuterium in dense clouds is in HD, whose fundamental transition lies at 112 μm.

2.3. Gas-Phase Bands

Fundamental vibrational transitions of important molecules such as H_2O, CH_4, C_2H_2, HCN, and CO_2 occur at mid-IR wavelengths. This is the only way to observe symmetric molecules like CH_4 and C_2H_2 that have no dipole moment and thus cannot be observed through rotational transitions at millimeter wavelengths. Also, CO_2 and H_2O are so abundant in Earth's atmosphere that their interstellar lines can only be detected from space. The pure rotational transitions of H_2O, OH and CO lie at far-IR wavelengths. Together, the vibrational and rotational lines are good probes of the physical conditions of the gas, its cooling and its chemistry.

2.4. PAHs

The C—C and C—H stretching and bending modes of polycyclic aromatic hydrocarbons (PAHs) at 6.2, 7.7, 8.6, 11.3, ... μm dominate the mid-IR spectra of many objects and are indicators of the presence of complex carbonaceous material excited by UV radiation.

---

[3] The following nomenclature is used: X refers to the atom or molecule as a chemical species, [X] indicates the abundance of the element in all forms with respect to total hydrogen, and [X I] 100 μm denotes its forbidden mid- or far-IR line.

TABLE 2 Selected mid- and far-IR spectral features observed by *ISO*

Category	λ (μm)	Species/line	Diagnostic[a]	PDR	Shock	Embedded YSO	Disk
Atoms	25.2	[S I]	Shock versus photon heating	−	+	−	−
	34.8	[Si II]		+	+	−	−
	63.2	[O I]		+	+	+	−
	145.5	[O I]		+	+	+	−
	157.7	[C II]		+	+	+	?
H_2	6.9	$7 \rightarrow 5$	Mass and temperature of warm gas, shock versus photon heating	+	+	−	−
	8.0	$6 \rightarrow 4$		+	+	−	−
	9.7	$5 \rightarrow 3$		+	+	+	−
	12.2	$4 \rightarrow 2$		+	+	+	−
	17.0	$3 \rightarrow 1$		+	+	+	?
	28.2	$2 \rightarrow 0$		+	+	+	?
HD	19.4	$6 \rightarrow 5$	[D]/[H]	−	+	−	−
	112.0	$1 \rightarrow 0$		+	−	−	−
Gas-phase molecules	6.0	H_2O	Temperature + density, ice evaporation, organic chemistry, depletion	−	+	+	−
	7.7	CH_4		−	−	+	−
	13.7	C_2H_2		−	−	+	−
	14.0	HCN		−	−	+	−
	15.0	CO_2		−	+	+	−
	104.4	CO $25 \rightarrow 24$		−	+	+	−
	108.1	o-H_2O $2_{21} - 1_{10}$		−	+	+	−
	119.3	OH $^2\Pi_{3/2}$ $\frac{5}{2} \rightarrow \frac{3}{2}$		−	+	+	−
	130.4	CO $20 \rightarrow 19$		−	+	+	−
	138.5	p-H_2O $3_{13} - 2_{02}$		−	+	+	−
	162.8	CO $16 \rightarrow 15$		−	+	+	−
	174.6	o-H_2O $3_{03} - 2_{12}$		−	+	+	−

	179.5	o-H_2O $2_{12} - 1_{01}$		−	+	+	−
	186.0	CO 14 → 13		−	+	+	−
PAHs	3.3, 6.2, 7.7,	C-H and	Carbonaceous material,	+	−	−	+
	8.6, 11.3, 12.7,	C-C modes	UV radiation	+	−	−	+
	14.2, 16.2			+	−	−	+
Silicates	9.7		Bulk of dust	−	−	+	+
(amorphous)	18.0			−	−	+	+
Silicates	11.3, 16.4, 23.9,	Forsterite	Mineralogy, grain growth,	−	−	−	+
(crystalline)[b]	27.7, 33.8, 69		and processing/heating;	−	−	−	+
	18.5, 21.5, 24.5	Enstatite	Solar System connection	−	−	−	+
	8.6	Silica		−	−	−	+
	65	Diopside		−	−	?	?
Oxides	11.6	Al_2O_3	Solar System connection	−	−	−	+
	23	FeO		−	−	−	+
Sulfides	23.5	FeS		−	−	−	+
Carbonates	92.6	Calcite		−	−	?	−
Ices	4.27	CO_2	Volatile solids, organic	−	−	+	−
	4.38	$^{13}CO_2$	chemistry, thermal	−	−	+	−
	4.67	CO	history;	−	−	+	−
	6.0, 13	H_2O	Solar System connection	−	−	+	−
	6.85	$CH_3OH + NH_4^+$?		−	−	+	−
	7.7	CH_4		−	−	+	−
	15.2	CO_2		−	−	+	−
	44, 63	H_2O (cryst.)		−	−	+	+

[a] Diagnostic properties of category of species; individual species or lines probe a subset of these properties.

[b] Position may vary depending on composition.

2.5. Solid-State Vibrational Bands

The characteristic vibrational bands of ices, silicates, oxides, carbides, carbonates, and sulfides occur uniquely at IR wavelengths. They can be used as diagnostics of heating as well as grain growth. Solid-state species can be distinguished from gas-phase molecules because their bands lack the characteristic rovibrational structure and are broadened (see Figure 4).

Not all features listed above have been observed with all *ISO* instruments. In general, the detection of intrinsically narrow gas-phase lines in emission or absorption against a strong continuum such as Orion-KL required the highest spectral resolution provided by the Fabry-Perots of the SWS and LWS. For most other sources, sensitivity considerations dictated the use of the grating. The SWS spectral resolving power of 1000–2500 was particularly well matched to that needed to resolve the solid-state features and PAH bands, and analyze their substructure. At the low spectral resolving power provided by CAM-CVF and PHOT-S, the PAHs and broad solid-state bands are readily detected in much weaker sources than accessible with the SWS, but the analysis is limited because the profiles are unresolved. Strong gas-phase lines are only detected with CAM-CVF if the continuum emission is nearly absent, such as in shocks or PDRs.

The main limitations of the *ISO* data are their relatively low spatial and spectral resolution compared with modern ground-based telescopes. *ISO*'s telescope was only 60 cm, with spectrometer apertures ranging from $20''$ to $>1'$. This means that the different physical components associated with star formation (envelopes, outflows, disks) are often unresolved and blurred together. For extended sources, aperture changes cause jumps in the fluxes with wavelength. The spectral resolution was generally insufficient to obtain kinematic information.

In Sections 3–7, each of the species from Table 2 is discussed in detail, focusing on their spectroscopy. Subsequently, the features are put in the context of the different physical regions associated with star formation—PDRs, shocks, protostellar envelopes, and circumstellar disks—illustrating their diagnostic capability and *ISO*'s contribution to our understanding of physical and chemical processes.

3. GAS-PHASE MOLECULES AND THEIR CHEMISTRY

Although hampered by limited spectral resolution, the SWS and LWS have observed many gas-phase species. *ISO*'s main contributions have been of three types: (*a*) detections of new interstellar molecules not seen prior to *ISO* (e.g., CO_2, HF, CH_3) (Figure 5), (*b*) IR detections of molecules seen previously at other wavelengths (e.g., H_2O, SO_2, HD), and (*c*) IR bands of molecules observed previously from the ground or *KAO* (e.g., H_2, CH_4, C_3, C_2H_2, OH).

3.1. New Detections

Searches for gaseous CO_2 formed one of the main astrochemical goals of the SWS. This molecule is potentially one of the more abundant carbon- and

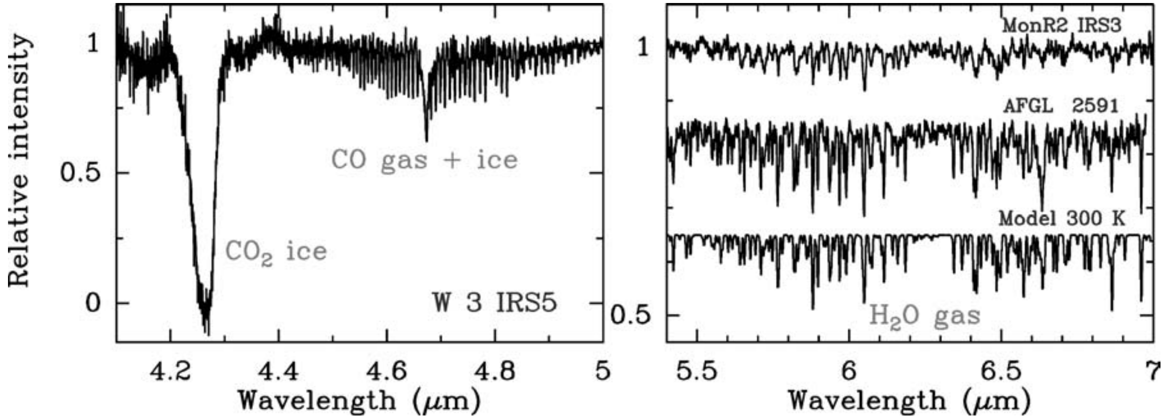

Figure 4 Normalized SWS spectra toward massive protostars showing absorption by various species: CO$_2$ ν_3 and CO ν_1 bands (*left panel*) and H$_2$O ν_2 band (*right panel*). The spectra in the right panel have been shifted vertically for clarity. Gas-phase molecules show sharp unresolved rovibrational lines in a characteristic pattern, whereas ices have a single broad absorption (Based on van Dishoeck 1998, Helmich et al. 1996, and Boonman & van Dishoeck 2003c).

oxygen-containing species, but ground-based searches were limited to the chemically related species $HOCO^+$. Detection of the CO_2 ν_2 band at 14.98 μm was reported by van Dishoeck et al. (1996) and confirmed by van Dishoeck (1998), Dartois et al. (1998b), and Boonman et al. (2003b,c) in a variety of star-forming regions. The inferred abundances with respect to H_2 are typically $\sim 2 \times 10^{-7}$, up to two orders of magnitude lower than those of solid CO_2 in the same regions (see Section 4). The line profiles indicate that the abundances can be a factor of 10 higher in warm gas at $T > 300$ K, whereas they are at least an order of magnitude lower in shocks. This chemistry is not yet fully understood.

Gas-phase CH_3 has been detected with the SWS through its ν_2 bending mode lines at 16.0 and 16.5 μm along the line of sight toward Sgr A^* with an abundance of $\sim 10^{-8}$ (Feuchtgruber et al. 2000). This molecule is an important building block in the formation of small hydrocarbon molecules. Together with observations of CH, CH_4, and C_2H_2 along the same line of sight, it forms a good test of basic gas-phase astrochemistry networks in diffuse and translucent clouds.

HF is interesting because it is the main reservoir of fluorine in dense molecular clouds and thus a direct measure of the fluorine depletion, supposedly characteristic of other species. The detection of the HF $J = 2-1$ line at 121.7 μm in absorption toward Sgr B2 by Neufeld et al. (1997) implies an abundance of $\sim 3 \times 10^{-10}$, indicating that only $\sim 2\%$ of the fluorine is in the gas-phase.

A new band at 57.5 μm has been reported by Cernicharo et al. (2002) toward Sgr B2 and may be attributed to either C_4 or C_4H. If ascribed to C_4, this would be the first detection of this molecule in outer space, at an abundance comparable to that of C_3. The latter molecule has been seen toward Sgr B2 through many LWS lines by Cernicharo et al. (2000a), with an abundance of $\sim 3 \times 10^{-8}$.

Several other new molecules have been detected in the envelopes around late-type stars and protoplanetary nebulae. Although not formally part of this review, the exciting SWS discoveries of C_6H_6 (benzene), C_6H_2, C_4H_2 (Cernicharo et al. 2001a), and C_2H_4 (Cernicharo et al. 2001b) toward CRL 618 should be mentioned.

3.2. Other Molecules

Most interstellar molecules with dipole moments are detected through their pure rotational emission lines at millimeter wavelengths. Complementary IR absorption data provide valuable constraints on the physical structure and geometry of the region. Using *ISO*, this has been possible for a few species, most notably HCN (Lahuis & van Dishoeck 2000; see also ground-based observations by Evans et al. 1991) and SO_2 (Keane et al. 2001a). In both cases, the inferred abundances from the IR data are two orders of magnitude higher than those obtained from the millimeter lines. Because the pencil-beam absorption data are more sensitive to the warm gas close to the protostar, the natural conclusion is that the abundances jump by a factor of ~ 100 in the inner region of the envelope owing to a combination of ice evaporation and high-temperature gas-phase chemistry (Figure 6) (Boonman et al. 2001).

Molecules without a permanent dipole moment observed with *ISO* include CH_4 (e.g., Boogert et al. 1998) and C_2H_2 (e.g., Lahuis & van Dishoeck 2000, Boonman et al. 2003c). Both species have been detected from the ground, but *ISO* allowed surveys in a larger number of sources. Analysis of the strong C_2H_2 Q−branch profiles gives rotational temperatures up to 1000 K. These temperatures correlate well with those of CO and other temperature tracers, indicating that C_2H_2 is a good probe of the inner envelope.

Higher rotational lines of NH, NH_2, and H_3O^+ have been seen in absorption with the LWS toward Sgr B2 (Cernicharo et al. 2000a; Goicoechea & Cernicharo 2001a,b). Together with the detection of a wealth of far-IR lines of hot NH_3 (Ceccarelli et al. 2002a), this allows tests of the basic nitrogen gas-phase chemistry. The interpretation is complicated, however, by the presence of many absorption components along the line of sight, including diffuse clouds, a warm dense envelope and a newly revealed layer of hot shocked gas. Several other molecules including SH, H_2O^+ and CH_2 have been searched for but not detected (Cernicharo et al. 2000a). The analysis of the full Sgr B2 Fabry-Perot spectrum is still in progress and may lead to further discoveries in this spectral gold mine. Higher-lying pure rotational transitions of CO^+ have been seen with the LWS toward the low-mass protostar *IRAS* 16293-2422 by Ceccarelli et al. (1998b), where its high abundance indicates either the presence of a dissociative shock or the importance of UV or X rays in the chemistry.

3.3. H_2 and HD

Interstellar H_2 is commonly observed through UV absorption lines in diffuse gas, and through near-IR emission lines in warm clouds, but only a few mid-IR pure rotational lines had been seen prior to *ISO* (e.g., Parmar et al. 1991). As discussed in detail in Sections 7 and 8, the SWS has routinely observed many H_2 pure rotational lines in a variety of regions, providing an excellent new probe of their physical conditions. The detection of the fundamental $J = 2 \rightarrow 0$ line at 28.22 μm was first reported by Valentijn et al. (1996) in the galaxy NGC 6946, and was subsequently seen in several galactic sources. This line probes the bulk of the warm gas at a temperature that is often lower than that inferred from the higher-lying H_2 lines.

Like H_2, interstellar HD has been observed through ultraviolet absorption lines prior to *ISO*, but only in diffuse clouds where the bulk of the deuterium is still in atomic form. The LWS has allowed the first detection of the fundamental HD $J = 1 - 0$ line at 112 μm in emission in a dense cloud in Orion where most of the deuterium is in molecular form (see Figure 5) (Wright et al. 1999). In addition, the higher-lying HD $J = 6 - 5$ line at 19.4 μm has been seen with the SWS in the Orion shock (Bertoldi et al. 1999). Together with observations of the pure-rotational H_2 lines, an accurate HD/H_2 abundance—and thus [D]/[H] abundance—can be derived. For both sources, a [D]/[H] ratio of (0.5–1.0) $\times 10^{-5}$ has been found, up to a factor of two lower than the [D]/[H] ratio of $(1.5 \pm 0.1) \times 10^{-5}$ measured in local diffuse clouds (Moos et al. 2002). The lower [D]/[H] ratio in an active star-forming region like Orion may be evidence of deuterium destruction by nuclear burning since its creation in the Big Bang. The HD 112 μm line has also been reported in emission in Sgr B2 (Polehampton et al. 2002) and in absorption toward W 49 (Caux et al. 2002). In these latter cases, H_2 is not observed directly and the determination of [D]/[H] is complicated by the fact that alternative tracers of H_2, in particular CO, may be significantly frozen out onto grains.

3.4. H_2O, OH, and O

Various H_2O lines have been seen prior to *ISO* from the ground and *KAO* at radio and millimeter wavelengths, but in virtually all cases these observations concern maser transitions. *ISO* has opened up a flood of data on thermal H_2O lines, either in emission or absorption, allowing much more accurate determinations of the H_2O abundance and excitation. Pure rotational emission and absorption lines at 25–200 μm have been seen with the LWS (e.g., Liseau et al. 1996, Cernicharo et al. 1997, Harwit et al. 1998) and SWS (Wright et al. 2000), and vibration-rotation lines at 6 μm with the SWS (e.g., Helmich et al. 1996; Dartois et al. 1998b; González-Alfonso et al. 1998, 2002; Moneti & Cernicharo 2000) (see Figure 4). Large variations in the H_2O abundances are found, ranging from $<10^{-8}$ in the coldest clouds to $>10^{-4}$ in warm gas and shocks, illustrating the extreme sensitivity of this molecule to the physical conditions. These variations can be explained by freeze-out of water at the lowest temperatures, ice evaporation at warmer temperatures ($\gtrsim$90 K), and gas-phase reactions driving most of the oxygen into water at high temperatures ($\gtrsim$230 K) (the geometry of the region is summarized in Figure 6) (Section 9.2).

The chemically related OH molecule has been detected through its pure rotational far-IR transitions in various objects (see Section 8), most prominently in absorption toward Sgr B2 (Goicoechea & Cernicharo 2002). Along this line of sight, [O I] 63 μm absorption has been seen as well, both with the LWS grating (Baluteau et al. 1997) and the LWS Fabry-Perot (Lis et al. 2001, Vastel et al. 2002). The conclusion from both sets of data is that the bulk of the gas-phase oxygen is in atomic form with O/CO $\approx$ 3–9, consistent with previous *KAO* results for DR 21 by Poglitsch et al. (1996). Even higher O/CO ratios have been inferred for W 49N by Vastel et al. (2000) and for the cold cloud L1689N by Caux et al. (1999). Although care should be taken in analyzing highly optically thick, potentially self-absorbed [O I] emission lines, the inferred high atomic oxygen abundances are consistent with nondetection of O_2 by the *SWAS* (Goldsmith et al. 2000).

4. INTERSTELLAR ICES

Interstellar H_2O ice was detected at 3 μm by Gillett & Forrest (1973), and the study of ices has subsequently been pursued from the ground and with the *KAO* (e.g., Willner et al. 1982). *ISO* has doubled the number of detected ice bands, bringing the current total to nearly 40 features. Most of the bands are observed in absorption arising in the cold outer envelopes of high-mass protostars (see Figures 6 and 7), but *ISO* has also allowed the first glimpse of ices toward low-mass objects (Cernicharo et al. 2000b; see Figure 2). The absorptions are deep: the total integrated optical depth is often larger than that of the 9.7 and 18 μm silicate absorptions and can amount to more than 50% of the total integrated flux. Only a few windows between the ice bands remain to probe close to the protostar. Ice bands are also seen with the LWS, in absorption toward protostars at 44 μm (Dartois et al. 1998a) and in emission in disks around young stars at 44 and 63 μm (Malfait et al. 1998, 1999; Creech-Eakman et al. 2002) and one shock (Molinari et al. 1999). In the latter cases, water ice is in its crystalline form rather than in the amorphous phase, which is thought to dominate most of interstellar ice. In terms of abundances, the amount of ice (mostly H_2O) can be comparable to that of the most abundant gas-phase molecule containing heavy atoms (CO), making it the second most abundant species after H_2 in cold clouds. Thus, a good understanding of the processes involving ices is highly relevant to understanding the physical and chemical characteristics of star-forming regions. Conversely, because ices are such a major component and show large variations in abundances and profiles, they are particularly powerful diagnostics of changes in environment. Recent reviews on interstellar ices and summaries of *ISO* data are given by Schutte (1999), Ehrenfreund & Schutte (2000), Boogert & Ehrenfreund (2004), and Gibb et al. (2004).

ISO's main contribution to the study of ices has been in two areas: (*a*) the first complete inventory of the main ice features and (*b*) clear evidence that changes in profiles and abundances can trace the gradual heating of protostellar envelopes.

4.1. Inventory of Ice Features

Table 2 and Figure 7 show a number of features with their identifications (see Boogert & Ehrenfreund 2004 for a complete list). Several of them are securely identified on the basis of multiple vibrational modes and isotopic bands, such as H_2O, CO, CO_2, and CH_3OH. For example, Dartois et al. (1998a) fit five H_2O bands simultaneously. Cleanly isolated single bands such as those due to solid CH_4 at 7.67 μm and OCS at 4.92 μm can also be confidently assigned if they are well matched by laboratory spectra. The identification of other species like H_2CO and NH_3 is more problematic because all their strong vibrational modes are blended with those of other species.

High-quality SWS profiles of the 6.0 and 6.8 μm bands—prominent toward all ice sources—show that they are clearly composites of several features (Schutte et al. 1996, Keane et al. 2001b). A good fit to the 6.0 μm band requires not only H_2O (known to be present from the 3 μm band), but also H_2CO at 5.85 μm and/or HCOOH at 5.83 μm to fit the blue wing and NH_3 at 6.15 μm or some carbonaceous material to fit the red wing. The 6.85 μm feature is still not firmly identified, although NH_4^+ is a plausible candidate and CH_3OH a minor contributor

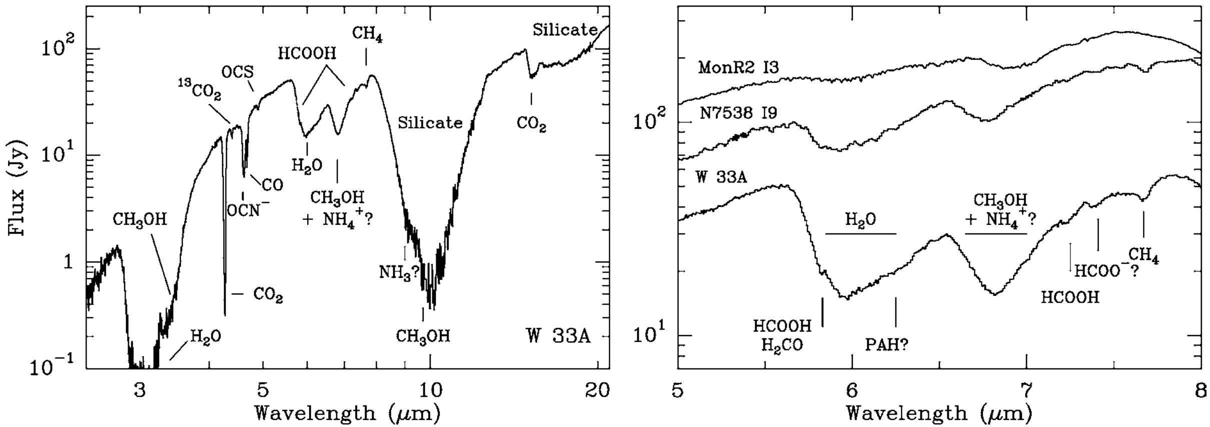

Figure 7 SWS spectrum of the embedded massive protostar W 33A, illustrating the wealth of ice features observed by *ISO* (Gibb et al. 2000). Blow-ups of the 5–8 μm region are shown for W 33A, NGC 7538 IRS9 (shifted in flux for clarity) and Mon R2 IRS3. Note the shift in the 6.85 μm band toward longer wavelengths for warmer sources like Mon R2 IRS3 (Keane et al. 2001b).

(Demyk et al. 1998, Keane et al. 2001b, Schutte & Khanna 2003). An empirical decomposition of the profile shows two components with fixed position and widths, whose relative intensities change with temperature of the source (see Figure 7).

The shape, exact position, and intrinsic strength of each band depend on the chemical environment of the molecule. For example, the position of the CO_2 stretching mode shifts by 20 cm^{-1} and its width broadens by a factor of two when CO_2 is mixed with H_2O ice rather than in its pure form. Analysis of the band profiles has led to a picture of layered ices, in which some molecules (e.g., CO) are not mixed with H_2O (Tielens et al. 1991). Ice profiles of crystalline material can be distinguished from their amorphous counterparts by being sharper and redshifted. Laboratory simulations of astrophysically relevant ice mixtures have been essential to provide the basic data to quantitatively analyze the ice bands (e.g., Hudgins et al. 1993; Gerakines et al. 1995; Ehrenfreund et al. 1996, 1997a).

A number of weak minor features have been found in the 7–8 μm region. Schutte et al. (1999) and Keane et al. (2001b) suggest HCOOH and $HCOO^-$ or CH_3HCO as plausible identifications. The presence of ions such as NH_4^+, OCN^- and $HCOO^-$ has been subject to considerable debate over the past 20 years, with the major controversy centering around the charge balance in the ice (not all counter ions have been found) and the constancy of the position of the observed ionic features. Schutte & Khanna (2003) show that heavier counterions have only weak spectral features and likely remain undetected, whereas the observed 6.85 μm shift is well reproduced in the laboratory by heating NH_4^+-containing ices.

Upper limits can be just as interesting as detections. The region between 5.0 and 5.8 μm (shown in Figure 7) is remarkably void of features and places limits on minor ice constituents. For example, the absence of the 5.62 μm band of the simplest amino acid glycine puts a limit on its abundance of less than 0.3% with respect to H_2O ice (or $<3 \times 10^{-7}$ with respect to H_2). Boudin et al. (1998) have put significant upper limits on C_2H_6, C_2H_5OH, and H_2O_2. Solid HNCO, the likely precursor of OCN^- and widely observed in the gas in hot cores, absorbs at 4.42 μm and is undetected down to 0.5%. In these regions, the confusion limit has certainly not yet been reached and higher S/N data may reveal new weak bands. Similarly, very few bands have been seen superposed on the strong continuum longward of the 9.7 μm silicate band, with the strong CO_2 bending mode at 15 μm being the notable exception.

Searches for absorption by more complex solid organic material are of obvious interest as a link with the large organic gas-phase molecules observed toward high-mass protostars. PAHs have been proposed to contribute to the red wing of the 6.0 μm absorption. Refractory organic residues, put forward by Greenberg et al. (1995) as resulting from UV processing of ices, have been suggested as an alternative explanation for the 6.0 μm excess absorption (Gibb & Whittet 2002).

Two very important molecules, O_2 and N_2, are largely invisible because their vibrational modes are dipole forbidden. When surrounded by other molecules, however, the transitions become weakly allowed. Searches for the N_2 band at 4.295 μm are hampered by overlap with the strong solid CO_2 stretching mode

(Sandford et al. 2001). Upper limits on solid O_2 feature at 6.45 μm, combined with an analysis of the effects of O_2 on the solid CO profiles, indicate that solid O_2 contains less than 6% of the total interstellar oxygen budget (Vandenbussche et al. 1999).

The isotopic species $^{13}CO_2$ and ^{13}CO have been detected and provide an independent determination of the [^{12}C]/[^{13}C] abundance gradient as a function of galactocentric radius as well as constraints on grain-shape effects that complicate the analysis of the main isotopes (Boogert et al. 2000a). The potential detection of solid deuterated water (HDO) by Teixeira et al. (1999) has not been confirmed by a reanalysis of the *ISO* data nor by independent ground-based data (Dartois et al. 2003).

4.2. Ice Abundances and Chemistry

H_2O ice is clearly dominant, with abundances of $10^{-5} - 10^{-4}$ with respect to H_2, thus containing a significant fraction of the oxygen (van Dishoeck 1998). The combined contribution of CO and CO_2 is typically 10–30%, but may be as high as 60%. For some sources, especially the most massive protostars, other carbon-bearing species (CH_3OH, HCOOH, CH_4, and H_2CO) may add an additional 20–30%, bringing the total abundance up to ~50% of that of H_2O (Gibb et al. 2004). Nitrogen appears much less abundant in the ice. Although the amount of NH_3 ice is under debate for some sources, it is certainly less than 10% and often less than 5% of that of H_2O ice (e.g., Dartois & d'Hendecourt 2001, Taban et al. 2003). The NH_4^+ abundance may be of order 10% (Schutte & Khanna 2003), but this still makes the identified nitrogen content at least a factor of four less than that of carbon.

A striking aspect of the ice composition is its simplicity. Although there is some observational bias against detection of low-abundance complex molecules in ices, all of the identified species are those expected from hydrogenation and oxidation of the main species to be accreted from the gas, i.e., O, C, N, and CO (Tielens & Hagen 1982). Various groups (e.g., Tielens & Chanley 1987, Stantcheva et al. 2002) have attempted to model this grain-surface chemistry quantitatively with varying degrees of success.

The SWS has provided detailed inventories of ices in about 30 sources. The majority of them are high-mass protostars, with only a limited number of intermediate mass YSOs (LkHα 225: van den Ancker et al. 2000c; Elias 18, HH 100, R CrA: Nummelin et al. 2001; AFGL 490: Schreyer et al. 2002) and low-mass sources (Elias 29: Boogert et al. 2000b; L1551 IRS5: White et al. 2000; T Tauri: van den Ancker et al. 1999; see also van den Ancker 2000 for unpublished SWS results). Using the higher sensitivity provided by CAM-CVF, Alexander et al. (2003) surveyed 42 low-luminosity sources ($L < 100$ L$_\odot$), whereas PHOT-S observed a handful of cases (e.g., Feldt et al. 1998; Gürtler et al. 1996, 1999, 2002). Although the lower spectral resolution does not allow a decomposition of the intrinsically blended 6.0 and 6.8 μm profiles, their overall spectra look remarkably similar to those of the higher luminosity counterparts. The 6.8 μm feature clearly correlates with H_2O, confirming that it is largely due to an ice. Significant variations are found between different clouds. For example, YSOs in the Chamaeleon I cloud show very little ice absorption overall, whereas those in ρ Oph appear to have a lower H_2O ice abundance and a larger scatter in the CO_2/H_2O abundance ratio compared with, for example, Serpens and CrA. ρ Oph may be peculiar because it has a large foreground layer of molecular gas with $A_V \gtrsim 10$ mag that may be relatively poor in ices owing to its lower density and larger exposure to UV radiation (Boogert et al. 2002).

4.3. Heating and Processing of Ices

The 15 μm bending mode of solid CO_2 toward high-mass protostars shows considerable variation from source to source, with a pronounced double-peak structure and a red wing seen in some sources (de Graauw et al. 1996b, Gerakines et al. 1999). Extensive laboratory simulations show that these variations can be well reproduced by gradual heating of a mixture of H_2O, CO_2, and CH_3OH ices in roughly equal proportions (Ehrenfreund et al. 1998, Dartois et al. 1999). At higher temperatures, the laboratory ices appear to segregate, leading to near-pure H_2O and CO_2 structures. Although this explanation seemed far-fetched at first, it is corroborated by a wealth of other evidence. In particular, the profiles of solid $^{13}CO_2$ at 4.38 μm (Boogert et al. 2000a), H_2O at 3 μm (Smith et al. 1989), and the 6.8 μm feature (Keane et al. 2001b) show similar changes owing to heating. Moreover, these changes are well correlated with increased gas/solid ratios derived from *ISO* (van Dishoeck & Helmich 1996, Boonman & van Dishoeck 2003) (see Section 9.2) and submillimeter data (van der Tak et al. 2000a) as well as increased dust color temperatures derived from the 45/100 μm *ISO* flux ratios (Boogert et al. 2000a). Indeed, the predictive power of these heating indicators is large: If one of them is found, so are the others. The emission data refer to the entire source rather than absorption along the line of sight, indicating that the entire envelope undergoes global warming. Although geometry (e.g., where does the mid-IR continuum become optically thick?) and line-of-sight effects (e.g., absorption looking down the outflow cone) may play a role in individual cases, they cannot be responsible for these general trends. As discussed further in Section 9.2, the most likely scenario is that the higher temperatures are due to a decreased envelope mass relative to the source's luminosity, perhaps caused by the dispersion of the envelope with time.

The presence of some features, e.g., that owing to OCN^- at 4.62 μm, has often been cited as an indicator of energetic processing, i.e., changes induced in the ice matrix composition or profiles owing to UV or particle irradiation rather than thermal heating (e.g., Pendleton et al. 1999). There have been extensive laboratory studies of these processes (see Gerakines et al. 1996 for UV; Moore & Hudson 1998 for energetic particle bombardment), but no "smoking gun" has yet been found observationally. In particular, van Broekhuizen et al. (2004) show that the OCN^- data can be quantitatively reproduced by thermal acid-base reactions of HNCO with NH_3 starting at temperatures as low as 10 K.

5. POLYCYCLIC AROMATIC HYDROCARBONS

Broad, strong IR emission features at 3.3, 6.2, 7.7, 8.6, 11.3, and 12.7 μm from a variety of astronomical sources have been known since the 1970s and are commonly known as the unidentified IR (UIR) bands. These features coincide with the vibrational modes of aromatic materials (Duley & Williams 1981), with the preferred identification that of free-flying Polycyclic Aromatic Hydrocarbons (PAHs) (Léger & Puget 1984, Allamandola et al. 1985). The fact that the bands are detected far from any illuminating source with roughly the same intensity ratios as those close to bright stars proves that the carriers are excited nonthermally by single UV photons (Sellgren 1984) and are interstellar. Indeed, both CAM-CVF and PHOT-S as well as the *IRTS* have shown that the mid-IR spectra (and thus also the *IRAS* 12 μm emission) of even the most diffuse interstellar medium are dominated by PAH features (Mattila et al. 1996, Onaka et al. 1996, Boulanger et al. 2000, Kahanpää et al. 2003). Any large ($>$100 Å) grain does not become hot enough under these conditions to emit at mid-IR wavelengths, so the carriers must be small, of order 10 Å, and correspond to PAHs with 30 to a few hundred carbon atoms containing up to 10–15% of the available interstellar carbon. Larger PAH clusters are seen through the plateaus underlying the discrete features. PAHs have also been seen in absorption at 6.2 μm in the diffuse medium toward objects in the Galactic Center and several dusty late-type Wolf-Rayet stars (Schutte et al. 1998).

The main contributions of *ISO* in this area have been to (*a*) allow a systematic analysis of the spectral characteristics of PAHs, revealing many new weak features, subbands, and shoulders; (*b*) survey the similarities and differences between the features for a wide variety of sources, relating them to physical and chemical changes; and (*c*) extend PAH studies to more diffuse regions exposed to much lower intensity radiation fields (see above). PAHs have been detected in many interstellar *ISO* spectra, indicating that they are ubiquitous, abundant, and able to survive in a wide range of conditions. Deeply embedded YSOs and shocks are the only types of regions where PAH emission is not seen. Detailed reviews of *ISO* PAH results have been given by Tielens et al. (2000) and Peeters et al. (2004b).

5.1. PAH Spectroscopy

Figure 8 shows the rich PAH spectrum of the Orion Bar PDR. In addition to the main features, weaker bands or substructures can be found at 5.2, 5.7, 6.0, 7.2–7.4, 7.6, 7.8, 8.2, 10.8, 11.0, 11.2, 12.0, 12.7, 13.2, 14.5, and/or 16.4 μm, with a weak plateau between 15 and 20 μm (see also Moutou et al. 2000, van Kerckhoven et al. 2000). Assignments in terms of C—H and C—C stretches are indicated. The C—H out-of-plane bending modes at 11–14 μm are particularly useful to characterize the PAH edge structure because their position depends on the number of adjacent H atoms bonded to neighboring C atoms on the ring. Solo-CH groups at 11.3 μm are indicative of straight edges on compact condensed PAHs like circumcoronene, whereas trio-CH groups at 12.7 μm arise at corners and thus imply more irregular PAHs.

Heroic efforts in laboratory spectroscopy (e.g., Hudgins & Allamandola 1999, see review by Tielens & Peeters 2004) have led to a large database of PAH spectra of various sizes and charges. It is clear that no single species fits all the features, but Allamandola et al. (1999) have succeeded in reproducing *ISO* spectra with a reasonable mixture of a dozen neutral and positively ionized PAHs, where each UIR feature is due to a superposition of many vibrational bands. The fact that the relative band strengths do not appear to vary much between PDRs exposed to orders of magnitude different radiation fields has been used to argue that the UIR features cannot be due to such an extended family of PAHs whose composition must change with physical conditions (e.g., Boulanger et al. 1998, 2000). However, as long as the ratio of UV intensity over electron density G_0/n_e (see Section 7) is similar and $\leq 10^3$ cm^3, the spectra of a PAH family do not change much (Bakes et al. 2001, Li & Draine 2002).

The high-quality spectra allow strict limits to be placed on functional groups attached to the PAHs, e.g., $-CH_3$, $-OH$, $-NH_2$, and $-C{=}O$ groups are, at most, 1% relative to aromatic C. The absence of strong 3.4, 6.85, and 7.3 μm bands indicates that they do not contain large aliphatic moieties. The fact that the C–C stretch occurs at wavelengths as short as 6.2 μm may be indicative of nitrogen substitution in the ring: pure PAHs start absorbing at 6.3 μm. Deuterated PAHs, in which an aromatic H is replaced by a D, have possibly been detected through bands at 4.4 and 4.65 μm at high abundances, PAD/PAH >0.1, in two sources (Peeters et al. 2004a). Other forms of large carbon molecules, e.g., C_{60} or C_{60}^+, are not seen down to 0.3% of total carbon (Moutou et al. 1999a).

5.2. PAH Feature Variations

Whereas the CH 3.3 and 11.2 μm bands correlate well with each other over a wide range of conditions, significant variations in the relative strengths of the C–H and C–C features are found, both between different types of sources and at different positions within a source (e.g., Hony et al. 2001). An excellent example of the latter case is provided by the M17 PDR, where the ratio of the 11.2/6.2 μm ratio changes by more than a factor of two across the ionization front (Verstraete et al. 1996). Because the C–H modes have much lower intrinsic band strengths for ionized PAHs compared with neutral PAHs, whereas the opposite holds for the C–C-modes (shown in Figure 9), this variation reflects a change in the degree of ionization: at the H II region interface, the PAHs are more ionized than deeper in the molecular cloud where they are also rehydrogenated. The actual charge state depends on the ratio G_0/n_e and may include doubly or even triply ionized PAHs. The smaller PAHs may be destroyed by intense UV radiation inside the H II region (Verstraete et al. 2001), although observational evidence is still controversial (Abergel et al. 2003).

The positions of individual C—H modes are relatively stable with peak wavelengths, changing by at most 4–6.5 cm^{-1}. In contrast, the C—C modes at 6–9 μm vary by 25–50 cm^{-1}. Moreover, the variations in the different C—C profiles are linked to each other (Peeters et al. 2002a) (see Figure 9). Specifically, reflection nebulae and PDRs show a different 7.7 μm complex than isolated young stars and post-AGB stars. Some H II regions contain a 8.6 μm band that dwarfs the commonly much brighter 7.7 μm band. Whereas these changes clearly indicate variations in the composition of the PAH family in response to different physical conditions, the details remain to be understood, especially because few PAHs reveal strong spectral features longward of 7.7 μm in the laboratory.

5.3. Hydrogenated Amorphous Carbon

The C—H stretching mode of aliphatic (chain-like) hydrocarbons at 3.4 μm has been detected from the ground along many diffuse lines of sight with extinctions $\gtrsim$10 mag (e.g., Pendleton & Allamandola 2002). *ISO* has provided further contraints on the composition of this material by detecting new features at 6.85 and 7.25 μm toward the Galactic Center (Chiar et al. 2000). A good fit is obtained with Hydrogenated Amorphous Carbon (HAC) with $H/C = 0.5$, with little evidence for strong C=O modes that would be the relic of first-generation photoprocessed ices. The total amount of carbon locked up in this material is uncertain, but may be as much as 25%. The relation with the aromatic material in the diffuse medium and the transformation between the two forms of carbon remains to be clarified (e.g., Mennella et al. 2001).

6. SILICATES

The detection of strong features at 9.7 and 18 μm bands owing to the Si—O stretch and O—Si—O bending modes (Gillett & Forrest 1973), coupled with the almost complete absence of silicon, magnesium, and iron from the interstellar gas, convincingly demonstrates that a large fraction of the interstellar refractory material is in the form of silicates. *ISO* has allowed researchers to (*a*) obtain high-quality silicate profiles of lines of sight through the diffuse interstellar medium and (*b*) reveal a surprisingly rich mineralogy of crystalline silicates in material around young and old stars.

6.1. Amorphous Silicates

The 9.7 and 18 μm silicate bands are the deepest broad absorption features seen in *ISO* spectra toward embedded YSOs and background stars and are found to be very smooth. Demyk et al. (1999) fit the 9.7 and 18 μm bands for dense cloud material toward protostars with amorphous, porous pyroxenes ($Mg_xFe_{1-x}SiO_3$) with some admixture of aluminum in the silicates. Kemper, Vriend & Tielens (2004) obtained a good fit for the diffuse cloud 9.7 μm band toward Sgr A* with ~0.1 μm-sized amorphous silicates consisting mostly of amorphous olivine (~85%; $MgFeSiO_4$) with a small admixture of amorphous pyroxene (~15%). The limits on the degree of crystallinity are very strict, $<$1–2% in the case of dense clouds, and $<$0.4% for the more diffuse medium. Alternative fits by Bowey & Adamson (2002) with a complex mixture of crystalline material, constructed such that the many individual peaks blend into a smooth broad profile, seem less likely.

This low degree of crystallinity is in stark contrast with the significant amounts of crystalline material of typically 10–20% (with extremes up to 75%) found in the envelopes around evolved stars (e.g., Molster et al. 2002). Because these stars are thought to provide a significant fraction of the interstellar dust, the observed lack of crystallinity has important implications. One explanation is that amorphization due to energetic particles occurs in the interstellar medium on a timescale of $<$10 Myr, significantly shorter than the dust destruction timescale. Another possibility is that the production rates of amorphous silicates from other sources (e.g., supernovae) are much larger than thought before, diluting the crystalline silicate fraction originating from post-AGB stars.

6.2. Crystalline Silicates

In dense clouds close to hot stars, the dust particles become sufficiently warm at a few hundred K to show silicate bands in emission. *ISO* examples are provided by Jones et al. (1999) for M 17, Cesarsky et al. (2000a) in Orion, Lefloch et al. (2002) in the Trifid nebula, and Onaka & Okada (2003) for Carina and S 171. Although the bulk of the emission is thought to be due to small amorphous grains, some evidence for discrete features has been claimed. For example, Onaka & Okada found a feature at 65 μm that may be due to diopside, a calcium-bearing crystalline silicate. Ceccarelli et al. (2002c) showed that the spectral energy distribution of one protostar, NGC 1333 IRAS4, has excess emission at 95 μm, which may be ascribed to calcite—a calcium-containing carbonate. Calcite has also been found in two planetary nebulae by Kemper et al. (2002) and is common in meteorites, with abundances of ~0.3–1% of the (warm) dust mass in all types of objects. If confirmed, the detection of calcite in a cold protostellar envelope would be additional evidence that its formation does not require liquid water.

The richest silicate spectra are found in disks around young and old stars. A survey by Meeus et al. (2001) of a sample of isolated young intermediate mass stars away from molecular clouds—the so-called Herbig Ae stars (Waters & Waelkens 1998)—reveals silicate emission for at least 70% of the sources. In some objects, only the broad 10 and 18 μm bands attributed to amorphous silicates are seen, whereas others reveal a large variety of narrower solid-state emission bands (shown in Figure 10). The most spectacular example is provided by HD 100546, which shows at least 8 bands that can be ascribed to forsterite, Mg_2SiO_4 (Waelkens et al.

1996, Malfait et al. 1998). Other minerals identified in disks around Herbig Ae stars include enstatite ($MgSiO_3$; Bouwman et al. 2001), hydrous silicates such as montmorillonite (Malfait et al. 1999), silica (SiO_2; Bouwman et al. 2001), metallic iron and iron oxide (van den Ancker et al. 2000a, Bouwman et al. 2000), although the FeO 23 μm feature can also be ascribed to FeS (Keller et al. 2002). The necessary laboratory spectroscopy is summarized in Henning (2003). Long wavelength data are often essential to make firm identifications (Figure 11), but LWS spectra exist for only a few sources. Typical mass fractions of the crystalline material are 5–10% compared with amorphous olivine, with a few percent of silica. Several spectra also show features due to PAHs (see Section 5) and crystalline H_2O ice (see Section 4), some of which may be blended with the crystalline silicate bands. Remarkably, no trend has been found between the age of the star and the presence of crystalline silicate or PAH material over the 0.1–10 Myr range.

Although not related to age, the 10 μm silicate profiles do show variations from source to source and are significantly different from those found in the diffuse medium (Section 6.1). In Figure 12, a collection of silicate profiles is presented, arranged such that the peak emission occurs at progressively longer wavelengths. These shifts can be caused by two effects, collectively called dust processing: coagulation of grains resulting in larger average grain sizes and crystallization resulting in discrete peaks, for example, by forsterite at 11.3 μm. Bouwman et al. (2001) argue on the basis of correlations between features that grain growth from submicron- to micron-sized grains dominates the shift. The timescales for coagulation and annealing are not coupled, with crystallization having a longer timescale. The SiO_2 band at 8.6 μm may be a by-product of the annealing process leading to crystalline forsterite, as has been observed in the laboratory (Rietmeijer et al. 2002).

The absence of the 10 μm band in some sources is intriguing and may be due either to the absence of any small ($\lesssim$few μm) silicate grains or to low temperatures caused, for example, by shadowing (see Section 10). A recent reanalysis of the SWS spectrum of HD 100453 shows that both effects likely play a role (Meeus et al. 2002; B. Vandenbussche, C. Dominik, M. Min, R. van Boekel & L.B.F.M. Waters, submitted manuscript): features owing to large ($\sim$2 μm) crystalline forsterite grains are detected at longer ($>$30 μm) wavelengths, but no emission is seen at 11 μm.

Silicate emission from disks around low-mass T Tauri stars has been observed with PHOT-S (Natta et al. 2000, Gürtler et al. 1999). Although the quality of the spectra is limited, broad amorphous silicate features from submicron-sized grains consisting of a mix of olivines and pyroxenes are found in all cases. There are hints of 11.3 μm crystalline forsterite and 8.6 μm silica features in some sources, but confirmation requires higher S/N and higher spectral resolution data. Indeed, crystalline silicates in disks around solar-mass stars have recently been found from ground-based data by Honda et al. (2003). Mid-IR spectroscopy of such objects is an obvious target for future space missions.

7. PHOTON-DOMINATED REGIONS

In photon-dominated or photodissociation regions (PDRs), far-UV photons (6–13.6 eV) control both the thermal and chemical structure of the neutral gas. Except for the densest shielded regions, the bulk of the molecular gas in our Galaxy and external galaxies has only a moderate opacity to UV radiation. Indeed, PDRs dominate the diffuse IR emission from molecular clouds, through conversion of the ambient UV photons to IR radiation from dust and gas. The study of PDRs was triggered by early airborne observations of strong far-IR atomic fine-structure lines (e.g., Melnick et al. 1979). Prominent [C II] 158 μm and [O I] 63 and 145 μm lines from regions like Orion stimulated the development of detailed PDR models (Tielens & Hollenbach 1985). Together with subsequent observations of UIR/PAH emission (see Section 5) and ground-based [C I] and high-excitation CO lines, a flurry of activity on PDRs resulted in the 1980s and 1990s. Comprehensive reviews have been given by Hollenbach & Tielens (1997, 1999).

PDRs have been widely observed with *ISO* using all four instruments. CAM images at 7 μm (dominated by PAHs) and 15 μm (dominated by small grains) beautifully reveal the cloud surfaces set aglow by the surrounding UV radiation (see Figure 1). Both CAM-CVF and PHOT-S have obtained spectra of the diffuse medium (Boulanger et al. 2000, Mattila et al. 1996). LWS and SWS spectra show a wealth of atomic fine-structure lines of neutral or singly ionized species, as well as the mid-IR H_2 lines. Bright PDRs studied with *ISO* spectroscopically include S 140 (Timmermann et al. 1996), NGC 2023 (Moutou et al. 1999b, Draine & Bertoldi 1999), NGC 7023 (Fuente et al. 1999, 2000), NGC 2024 (Giannini et al. 2000), W 49N (Vastel et al. 2001), S 106 (Schneider et al. 2003), S 125 (Aannestad & Emery 2001, 2003), S 171 (Okada et al. 2003), IC 63 (Thi et al. 1999), the Trifid nebula (Lefloch et al. 2002), and Trumpler 14 (Brooks et al. 2003).

Models have shown that the strength of the emission lines depends mainly on two parameters: the gas density n and the intensity of the incident radiation field, characterized by an enhancement factor G_0 compared with the standard interstellar radiation field. Here $G_0 = 1$ refers to an integrated ultraviolet (6–13.6 eV) intensity of 1.6×10^{-3} erg s^{-1} cm^{-2} (Habing 1968), a factor of 1.7 lower than the reference field by Draine (1978). Most of the PDRs mentioned above have densities of at least 10^4 cm^{-3} and radiation fields $G_0 > 10^3$. Because many of these bright PDRs have also been observed with the *KAO*, the *ISO* data have helped mostly to refine the physical structure of the models (e.g., more accurate density determinations, constraints on clumpy or layered structures) and geometry (e.g., inclination, face-on versus edge-on, 3D geometry). Care should be taken not to overinterpret the data, however. Comparison of results from different PDR codes shows differences in predicted line intensities up to a factor of two to three owing to different assumptions in the input data and chemistry. Also, some lines, in particular the [O I] 63 μm line, are optically thick so that model results are sensitive to the details of the radiative transfer and possible self-absorption by cold foreground gas.

The higher spatial resolution *ISO* data have confirmed earlier suggestions that most of the observed [Si II] 34.8 μm emission originates from the outer PDR layer with $A_V \leq 2$ mag rather than from any ionized gas in the region (e.g., Fuente et al. 2000, Lefloch et al. 2002), with the enhanced gas-phase silicon most likely owing to photodesorption of Si-containing grain-mantle material (Walmsley et al. 1999). Not all PDRs show [Si II] emission, however (Rosenthal et al. 2000).

The main new insights due to *ISO* have been (*a*) extension of PDR studies to the lower n and G_0 regime, (*b*) direct measurement of the efficiency of heating the gas through the photoelectric effect, and (*c*) detailed studies of the H_2 mid-IR pure rotational lines leading to new insights into the temperature structure and H_2 formation rate at high temperatures. PAHs are discussed mostly in Section 5.

7.1. Low-Excitation PDRs and the Gas Heating Efficiency

Low-excitation PDRs with $n \leq 10^4$ cm^{-3} and/or $G_0 < 100$ studied by *ISO* include L1457 (MBM12) (Timmermann et al. 1998), the S 140 extended region (Li et al. 2002), L1721 (Habart et al. 2001), ρ Oph main (Liseau et al. 1999), ρ Oph W (Habart et al. 2003), and a set of translucent clouds also studied by optical absorption lines (Thi et al. 1999). Cederblad 201 (Kemper et al. 1999, Cesarsky et al. 2000b) is an example of a PDR exposed to a cooler B9.5 star where the radiation field has fewer far-UV photons. The physical structure of these clouds is often well-characterized from complementary data, so that they form good tests of the basic PDR models. Although some *ISO* lines (e.g., [C II]) are well explained, others (e.g., H_2) cannot be reproduced with standard model parameters (see Section 7.2.3).

Comparison of the total intensity of the main cooling lines (principly [C II] 158 μm for the low-excitation PDRs) with the far-IR continuum gives directly the heating efficiency ϵ of the gas owing to the photoelectric effect. Assuming that the lines are optically thin, values ranging from 1–3% are obtained. These efficiencies are somewhat higher than the range of 0.1–1% found for a sample of higher n, G_0 PDRs by Stacey et al. (1991) with the *KAO* and that of 0.7% for S 106 studied with *ISO*. For very high values of G_0/n appropriate for clouds like W 49N, the photoelectric heating efficiency is clearly suppressed by an order of magnitude to (0.01–0.04)%. This is consistent with models by Bakes & Tielens (1994), who show that intense radiation results in more highly charged grains that have a larger barrier for the photoelectrons to escape. So far, W 49N is the only PDR for which such low efficiencies have been found. Even Trumpler 14, a PDR powered by at least 13 O stars, and 30 Doradus in the Large Magellanic Cloud (LMC), powered by at least 30 O stars, have efficiencies of 0.2–0.5% (Brooks et al. 2003). One possible explanation is that the ionization front in these cases is at such a large distance from the stellar cluster that the PDRs at the outer edges of the cloud do not have extreme parameters in terms of G_0 or n.

Habart et al. (2001) went one step further by spatially correlating the cooling lines with IR emission due to PAHs (4–12 Å; *IRAS* 12 μm), very small grains

(VSGs, 12–150 Å; *IRAS* 25 and 60 μm), and big grains (>150 Å; *IRAS* 100 μm). They conclusively showed that the PAHs are the most efficient heating agents, with $\epsilon_{\rm PAH} = 3\%$, $\epsilon_{\rm VSG} = 1\%$, and $\epsilon_{\rm BG} = 0.1\%$. Habart et al. (2003) found $\epsilon_{\rm PAH} = 4\%$ for the ρ Oph West cloud. Both studies also found evidence for an increase in the PAH abundance near the edge of the cloud, consistent with other studies based on *IRAS* and/or *ISO* imaging (e.g., Boulanger et al. 1990, Abergel et al. 2002).

7.2. H_2 Pure Rotational Lines

7.2.1. ROTATIONAL TEMPERATURES The H_2 pure rotational quadrupole lines are readily detected from bright PDRs, in spite of their small intrinsic Einstein $A-$values (see Figure 13). In contrast with the vibration-rotation lines at 2 μm seen from the ground, the lowest rotational levels are primarily excited by collisions in warm gas rather than by UV pumping (e.g., Black & van Dishoeck 1987, Sternberg & Dalgarno 1989, Draine & Bertoldi 1996). This is directly reflected in their excitation diagrams (see Figure 13, right), which show that the $v = 0$ rotational distribution is characterized by a temperature $T_{\rm rot} = 400$–700 K (e.g., Timmermann et al. 1996, Fuente et al. 1999, Wright 2000), much lower than the vibrational temperatures of $T_{\rm vib} \approx 2000$ K. The inferred $T_{\rm rot}$ for various PDRs are remarkably similar in spite of their different characteristics. It should be noted, however, that only a few sources have been studied in detail and that, in several cases, the integrations were not deep enough to reveal the lowest $J = 2 - 0$ line at 28.22 μm. Where detected, this line shows evidence for a lower temperature component with $T_{\rm rot} \approx 100$ K. It is interesting to note that the rotation diagrams derived from H_2 UV absorption line data of diffuse (e.g., Spitzer & Cochran 1973) (see Figure 13) and translucent (e.g., Snow et al. 2000) clouds are also similar. These data, which include the populations of the lowest two $J = 0$ and $J = 1$ levels, clearly reveal the multitemperature structure. Similar diagrams have been found for extragalactic regions in normal (e.g., Valentijn & van der Werf 1999) and starburst galaxies (e.g., Rigopoulou et al. 2002).

In spite of their simple appearance, the interpretation of these diagrams has to take account of several factors. First, the gas kinetic temperature varies rapidly through the PDR layer from a value of several hundred K at the edge to less than 30 K when $A_V > 1$ mag. The pure rotational H_2 lines arise primarily from the outer warm layer, but its temperature depends strongly on n and G_0, as well as the assumed PAH heating parameters (e.g., Kaufman et al. 1999). Second, only the lowest rotational levels are collisionally excited. For diffuse clouds, this holds only up to $J = 2$, whereas for denser PDRs like S 140 levels up to $J = 5$ may be populated by collisions. Finally, the rotational populations are affected by UV pumping in at least two ways: in an absolute sense by providing more population in the higher-J levels, and in a relative sense by the fact that the excitation rates out of the various J levels differ with depth into the cloud. No PDR model that fits all the *ISO* data and takes all these effects into account in a fully self-consistent manner has yet been published. For example, the excellent fits to the S 140 H_2

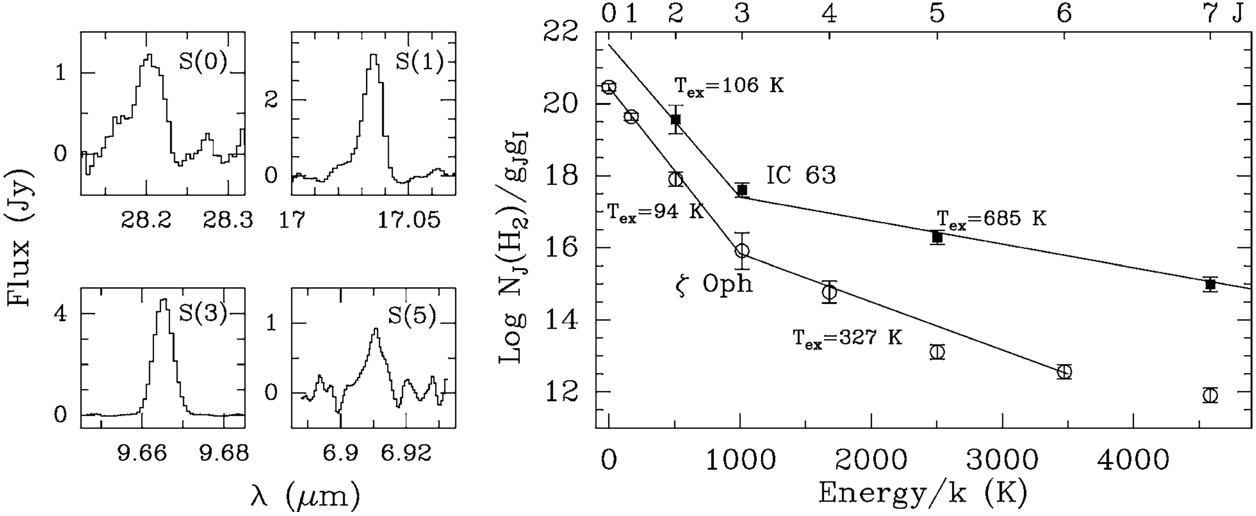

Figure 13 (*Left*) Pure rotational H_2 lines observed toward IC 63 with the SWS (Thi et al. 1999). (*Right*) H_2 excitation diagram for IC 63 compared with that derived from UV observations of the diffuse cloud ζ Oph (Spitzer & Cochran 1973). The statistical weights are $g_J = 2J + 1$ with $g_I = 1$ for para-H_2 and $g_I = 3$ for ortho-H_2.

data by Timmermann et al. (1996) use a fitted gas temperature profile rather than a computed one.

One general conclusion of all PDR models is that the gas temperature needs to be higher in the zone where H_2 is formed than can be explained by the standard gas heating and cooling processes. Draine & Bertoldi (1999) discuss possible remedies. In addition to changes in geometry and density structure, possible uncertainties in the microphysics include the H_2 inelastic collisional rate coefficients, the grain photoelectric heating efficiency, and an increased dust-to-gas ratio in the PDR zone due to an isotropic illumination of grains that causes them to drift through the gas. An additional option, namely an increased H_2 formation rate, is discussed below. Yet another explanation, namely that of weak shocks in diffuse gas, remains to be quantified.

7.2.2. ORTHO/PARA RATIO There has been significant confusion in the literature on the ortho/para ratio of H_2, with several claims of ortho/para ratios that are lower than the equilibrium value corresponding to the temperature derived from excitation diagrams (e.g., Fuente et al. 1999). As pointed out by Sternberg & Neufeld (1999), care has to be taken with such statements because a low ortho/para ratio in excited levels naturally results from the fact that the optical depth in the UV pumping lines is higher for the ortho- than for the para-H_2 lines (see their figure 5). None of the *ISO* data measure the bulk of ortho- and para-H_2, which resides in $J = 0$ and 1. Additional concerns are mentioned by Wright (2000). Nevertheless, some of these claims of nonequilibrium ortho/para ratios in high-temperature gas may be valid (see also Section 8), in which case they are interesting indicators of dynamical processes, such as the advection of colder gas into the PDR.

7.2.3. INCREASED H_2 FORMATION RATE Detailed studies of several well-characterized, low-excitation PDRs have shown convincingly that the intensities of the lowest H_2 lines cannot be reproduced with standard PDR parameters (e.g., Bertoldi 1997; Kemper et al. 1999; Thi et al. 1999; Habart et al. 2001, 2003; Li et al. 2002). The discrepancies are significant, at least an order of magnitude. Because the gas-grain drifts discussed above are not significant for these regions, the discussion has focused on two solutions: first, an increase in the photoelectric heating rate, for example, through a larger PAH or very small grain abundance; and second, an increase in the H_2 formation rate at high temperatures. A combination of these two solutions has the effect of moving the H–H_2 transition zone closer to the edge of the PDR where the temperatures are higher. The most quantitative study is by Habart et al. (2003, 2004), who show that for most (but not all) sources an increase in the H_2 formation rate by a factor of $\sim$5 at temperatures of a few hundred K is needed, compared with the standard rate of (3–4) $\times 10^{-17}$ cm^3 s^{-1} derived from UV absorption lines by Jura (1975) and Gry et al. (2002) for diffuse clouds.

Because the residence times of physisorbed H on grains at such high temperatures are much too short for H_2 formation to occur, this conclusion has fundamental implications for our understanding of basic molecule formation processes.

One possibility is that direct reactions of atomic H arriving from the gas on top of chemisorbed species dominate in an Eley-Rideal type process (see e.g., Duley 1996). Another option is that physisorbed H diffuses over the surface to find a chemisorbed H in a Langmuir-Hinshelwood-type process (Hollenbach & Salpeter 1971). Quantitative estimates of the rates of both processes have been made (Cazaux & Tielens 2002, Habart et al. 2004). The efficiencies depend sensitively on the number of chemisorbed sites and the activation energy barrier to molecule formation, both of which are uncertain.

8. SHOCKS

Shocks in molecular clouds can be caused by a large variety of processes including outflows and jets from young stars, supernovae, and expanding H II regions. Recent reviews of the theory of shocks have been given by Draine & McKee (1993) and Hollenbach (1997). In this section, *ISO* observations of well-characterized shocks away from the driving sources are discussed; those in the inner parts of protostellar envelopes are included in Section 9. The continuum emission due to warm dust offset from the YSOs is generally very low so that all lines are in emission (see Figure 2). Early models by Hollenbach et al. (1989) show that slow, nondissociative shocks have many strong diagnostic lines at IR wavelengths. In these so-called C-type shocks, the hydrodynamical variables change continuously and the maximum temperature is only 2000–3000 K, too low to dissociate molecules. In contrast, the temperatures in high-velocity J-type shocks jump to more than 10^5 K, and most of the emission is from atomic lines at UV wavelengths. Also, these shocks can cause shattering or nonthermal sputtering of grain cores, resulting in enhanced abundances of Si, Mg, Fe, and other grain constituents.

ISO's main contributions to the study of shocks have been to (*a*) characterize better the shock structure and physical conditions, especially those found in the slower shocks; (*b*) measure the total cooling power directly from observations, in particular the individual contributions from H_2O and H_2, and thus understand the overall energy budget; and (*c*) study global and systematic trends by observing much larger samples. A good overview has been given by Noriega-Crespo (2002).

The *ISO* data have also convincingly shown that all broad band emission from shocks is due to lines (e.g., Cesarsky et al. 1999). For example, the *ISO*-CAM 7 and 15 μm bands are dominated by the H_2 S(4) and S(1) lines, whereas the *IRAS* 12, 25, and 60 μm emission is due to H_2 S(2), S(0), and [O I] 63 μm, respectively.

8.1. Shock Structure and Physical Conditions

Shocks associated with outflows studied by *ISO* include Orion (Harwit et al. 1998, Rosenthal et al. 2000, Sempere et al. 2000, González-Alfonso et al. 2002), HH 1-2 (Cernicharo et al. 2000b, Lefloch et al. 2003, Cabrit et al. 2004), HH 7–11 (Molinari et al. 2000), HH 46 (Nisini et al. 2002), HH 52–54 (Liseau et al. 1996, Nisini et al. 1996), HH 80-81 (Molinari et al. 2001), Cep A West (Wright et al.

1996, Froebrich et al. 2002), Cep E (Moro-Martín et al. 2001, Smith et al. 2003), DR 21 (Wright et al. 1997), L1448 (Nisini et al. 1999a, 2000; Froebrich et al. 2002), B 335 (Nisini et al. 1999b), L1551 (White et al. 2000), NGC 1333 (Bergin et al. 2003) and a variety of other low-mass YSOs including L1157 (Giannini et al. 2001). Shocks associated with supernova remnants investigated by *ISO* include IC 443 (Cesarsky et al. 1999) and 3C 391, W 44, and W 28 (Rho & Reach 2003). In all types of shocks, molecular (H_2, CO, H_2O, OH) and atomic ([O I], [C II], [S I]) lines are often detected (Figures 14 and 15), although there are sources in which no molecular lines except H_2 are seen (e.g., L1551 IRS5 and HH 80-81).

In spite of the fact that the available diagnostics often differ depending on whether SWS, LWS, and/or CAM-CVF data are obtained, the conclusion is invariably that no single planar static shock can explain all the data. Specifically, the H_2 excitation and the presence of other molecules require a combination of slow ($<$20 km s^{-1}) and faster (30–50 km s^{-1}) C–shocks with different covering factors, whereas the atomic lines can only be explained with a high-velocity J–type shock (70–140 km s^{-1}). The estimated filling factors of the shocks are small, typically a few percent of the LWS beam. It is still unclear whether these different shocks can be combined in a single unified model. Attempts to do so include bow shocks with long flanks, where a broad distribution of shock speeds arises from the curvature (e.g., Froebrich et al. 2002), time-dependent C–shocks with embedded transient J–shocks (e.g., Chièze et al. 1998), or multiple shocks linked to multiple episodes of outflow activity (e.g., Nisini et al. 2000).

8.1.1. ATOMIC LINES, J-SHOCK DIAGNOSTICS A clear diagnostic of a fast dissociative J-shock is the [Ne II] 12.8 μm line, whose intensity is directly proportional to v_s. This line is commonly associated with high-mass YSOs, but has been detected in only one low-mass YSO (HH 1–2) (see Figure 2). The lack of [Ne II] or other highly ionized fine-structure lines toward low-mass YSOs, coupled with the detection of optical high-excitation lines, indicates that the area occupied by high-velocity $\sim$200 km s^{-1} shocks is small, typically $<1''$. Instead, van den Ancker et al. (2000b,c) show that [S I] 25.2 μm may be a better shock diagnostic. Another often-used probe is the [C II]/[O I] fine-structure line ratio, which is expected to be low in fast J-shocks. [C II] can also arise in PDRs, however, either from the surrounding molecular cloud emission or produced locally by the shock. Indeed, Molinari et al. (2001) and Molinari & Noriega-Crespo (2002) have argued that much of the observed [C II] emission in Herbig-Haro sources arises from PDRs at the walls of the outflow cavity. This radiation can also create a PDR in the quiescent gas ahead of the shock.

8.1.2. H_2 LINES, C-SHOCK DIAGNOSTICS As for PDRs, the pure rotational H_2 lines dominate the mid-IR spectra and are characterized by excitation temperatures of 700–1000 K. In contrast, the well-studied H_2 vibration-rotation lines usually give $T_{ex} = 2000$–3000 K. Many papers treat these two data sets separately, but the combined pure-rotation and vibration-rotation data observed with *ISO* clearly indicate that two excitation temperatures are common, with evidence for even higher excitation conditions (>10000 K) in some sources (Cep A: Wright et al. 1996; Orion: Rosenthal et al. 2000). The most impressive collection of H_2 lines is seen for Orion at the so-called Peak 1 (see Figure 3) (Rosenthal et al. 2000) and Peak 2 (C.M. Wright, private communication) positions, where 56 H_2 lines have been seen, including the $v = 0$ S(1) to S(25) lines with upper energy levels up to 42500 K. The detection of the S(25) line is particularly intriguing and may be indicative of nonthermal excitation processes, either by direct population of high-J levels during the formation of H_2 (so-called formation pumping) or by nonthermal collisions between ions and molecules in the shock. However, Le Bourlot et al. (2002) have recently re-evaluated the chemistry and excitation of H_2 in shocks using much improved H_2-H and H_2-H_2 collisional-rate coefficients, and concluded that the critical velocity at which H_2 is dissociated is significantly higher than previously thought. As a result, higher excitation of H_2 can result from thermal collisions only, and the Orion H_2 data can be reproduced with a two-component C–shock model without the need for nonthermal excitation processes. CAM-CVF images show that H_2 avoids the high-excitation optical knots and has a distribution more consistent with shocked gas swept up by the bow-shock (e.g., Cabrit et al. 1999, 2004; Larsson et al. 2002).

Theoretical calculations of the H_2 rotational excitation in various shock models give T_{ex} values of 200–540 K for J–shocks, but a much larger range of 100–1500 K for C–shocks (see figure 8 in van den Ancker et al. 2000b). T_{ex} does not depend much on density, but increases strongly with shock velocity. Thus, the observed range of T_{ex} discussed above naturally leads to at least two C–type shocks. Interestingly, the rather narrow range of T_{ex} predicted for J–shocks is similar to that found for PDRs (see Section 7.2.1). For PDRs, T_{ex} does not depend much on density and is a good diagnostic of the UV radiation field G_0. Except for the shock associated with T Tau (van den Ancker et al. 1999), however, no case of a fluorescent contribution to the H_2 shock excitation has been found. More recently, Cabrit et al. (2004) have stressed the use of the H_2 pure rotational lines to also constrain the transverse magnetic field strength and abundance of small grains, both of which affect the shock details.

Because the collisional rate coefficients of H_2 with H are significantly larger than those with H_2 or He, the H/H_2 ratio in the preshocked gas is critical in the models. In general, much better fits to the shock data are obtained if this ratio is $\sim$0.1, at least two orders of magnitude larger than that expected in dark clouds. For most shocks, the inferred ortho/para ratio is three, consistent with the warm conditions. The major exceptions are HH 54 (Neufeld et al. 1998) and HH 2 (Lefloch et al. 2003), where significantly lower ortho/para ratios of 1.2–1.6 are found. This low ratio is thought to be a relic of the earlier cold-cloud stage, where the timescale of the shock passage has been too short to establish an equilibrium ortho/para ratio. Thus, the ortho/para ratio can be used as a chronometer, indicating for HH 54 that the gas has been warm for, at most, 5000 years. Timmermann (1998) showed that the ortho/para ratio only attains the high-temperature equilibrium value of three for shock speeds greater than 20–25 km s^{-1}.

8.1.3. CO, H_2O, AND OH LINES, *C*-SHOCK DIAGNOSTICS The LWS spectra of shocks associated with nearby low-mass YSOs often contain several CO lines of comparable strengths, ranging from $J = 14$–13 up to 25–24 (see Figures 1 and 14). The excitation temperature of CO is generally somewhat lower than that of H_2. Comparison of the H_2O/CO luminosity ratio with shock models requires slow (10–20 km s^{-1}) *C*-type shocks. Because submillimeter CO line profiles often indicate the presence of much higher shock velocities, one interpretation is that the slow shocks are proceeding into a medium that has been put into motion by a previous generation of shocks. Indeed, Nisini et al. (1999, 2000) associate the strong molecular emission found for L1448-mm directly with the extremely high-velocity bullets seen in CO that move at speeds up to 200 km s^{-1}.

The most spectacular high-mass example is again provided by Orion, where Harwit et al. (1998) detected many H_2O emission lines resolved with the Fabry-Perot (see Figure 16). The observed line strengths are well reproduced by the *C*-shock model of Kaufman & Neufeld (1996) in which most of the gas-phase oxygen is driven into H_2O leading to an abundance of $\sim 5 \times 10^{-4}$. At shorter wavelengths, the pure rotational H_2O lines go from emission into absorption, at least in the direction of Orion-IRc2 (Wright et al. 2000). Not all shocks associated with high-mass YSOs resemble Orion, however, even when scaled for the larger distances: H_2O emission lines are usually not detected with *ISO*, indicating much smaller filling factors (Boonman et al. 2003a) (also see Section 9.2).

8.2. Gas Cooling in Shocks

The complete IR spectral coverage provided by the *ISO* spectrometers allows a direct determination of the contribution of each species to the cooling. Figure 15

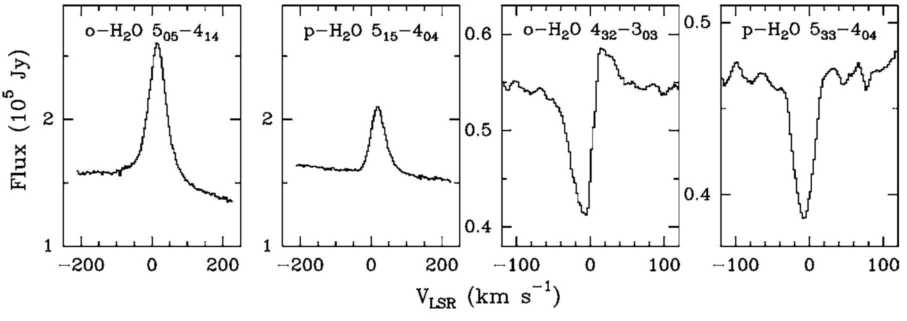

Figure 16 Examples of high-excitation emission and absorption lines of H_2O for the Orion shock observed with the LWS (o-H_2O $5_{05} - 4_{14}$ at 99.4931 μm, p-H_2O $5_{15} - 4_{14}$ at 95.6273 μm), and SWS (o-H_2O $4_{32} - 3_{03}$ at 40.6909 μm, p-H_2O $5_{33} - 4_{04}$ at 35.4716 μm) Fabry-Perot spectrometers (Harwit et al. 1998, Wright et al. 2000).

summarizes the results for a survey of embedded low-mass YSOs by Nisini et al. (2000, 2002). In many cases, H_2, CO, and H_2O have comparable contributions on-source with no single species clearly dominating. Off source, the H_2O contribution may be less. Together, the molecular lines can contain up to an order of magnitude more flux than the [O I] 63 μm line in the densest regions. The total observed cooling is often more than 50% of the mechanical power input of the shock, illustrating that the bulk of the kinetic energy is transformed into IR radiation.

In J-type shocks such as found in Herbig-Haro objects, the [O I] 63 μm line is usually the dominant coolant. In that case, its intensity is a direct measure of the mechanical luminosity, which in turn is related to the mass-loss rate. Values of 10^{-7}– 10^{-4} $M_\odot$ years^{-1} have been inferred this way, which correlate well with those derived from CO outflow maps indicating that the two phenomena are physically associated (Saraceno et al. 1999, Liseau et al. 1997).

9. EMBEDDED YOUNG STELLAR OBJECTS

ISO spectra taken at the position of the protostars themselves often show most of the spectral characteristics of cold and warm gas and dust discussed above, arising from different parts of the circumstellar environment (see Figure 6) (van Dishoeck et al. 1999). The cold outer envelope is seen prominently in ice absorption, whereas the PDRs and shocks are revealed through atomic, molecular, or PAH emission lines. As the protostellar evolution progresses, the relative contribution of each of these components changes. The main advances made possible by *ISO* have been to (*a*) quantify the relative contributions from different physical components and (*b*) establish a protostellar classification scheme based on mid- and far-IR spectroscopic features. For low-mass YSOs, this scheme complements and extends the Class 0, I, and II classification based on the spectral energy distribution (SED) (e.g., Lada 1999). For higher mass objects where the temporal ordering is much less clear (Churchwell 2002), IR spectroscopy is a powerful tool to characterize the earliest stages.

For sensitivity reasons, low-mass YSOs have been studied primarily with the LWS and CAM-CVF, whereas high-mass YSOs have been intensively observed with the SWS. These two sets of sources are therefore discussed separately, but within a common physical and chemical framework.

9.1. Low-Mass YSOs

9.1.1. LWS SURVEYS Giannini et al. (2001), Nisini et al. (2002), and Benedettini et al. (2003) summarized the LWS observations of 28 low-luminosity ($<$100 $L_\odot$) YSOs, consisting of 17 Class 0 and 11 Class I objects. Several of these objects have been studied individually in earlier papers, e.g., *IRAS* 16293-2422 (Ceccarelli et al. 1998a), B 335 (Nisini et al. 1999b), L1448-mm (Nisini et al. 2000), L1551 IRS5 (White et al. 2000), Serpens SMM1 (Larsson et al. 2002), and NGC 1333 *IRAS* 4 (Maret et al. 2002). The atomic [O I] 63 μm and [C II] 158 μm lines are detected in all sources and molecular lines in many cases, most prominently in the Class 0 objects. Specifically, CO, H_2O, and OH are detected in 94%, 70%, and 41% of the Class 0 sources, respectively, whereas CO and OH are seen in 64% and 27% Class I objects. No H_2O has been detected in any Class I source, except for T Tau (see below). The spectral evolutionary sequence is illustrated in Figure 14.

The total molecular cooling in Class 0 objects is significantly larger than that in Class I sources, whereas the atomic cooling through [O I] 63 μm is similar (see Figure 15). The total atomic + molecular line cooling $L_{\rm line}/L_{\rm bol} \approx 10^{-2}$ for Class 0 sources, whereas it is an order of magnitude lower for Class I objects. This decline is consistent with that in the outflow momentum flux, which in turn is thought to be related to the decay of the mass accretion activity with time (André et al. 2000).

Temperatures, densities, and column densities have been obtained by fitting molecular excitation models to the CO line ratios, giving values of a few hundred to $>$1000 K and densities of $10^5 - 10^6$ cm^{-3}. The filling factor of this warm and dense gas is small, $\sim 10^{-9}$ sr or a few hundred AU radius. Assuming that the physical parameters derived from CO are also valid for H_2O and OH, the inferred H_2O abundances range from 10^{-5} to a few $\times 10^{-4}$ and increase with the gas temperature. Where detected, the OH abundance is at least an order of magnitude lower than that of H_2O, of order $10^{-6} - 10^{-5}$. For Class I objects, the upper limit on the H_2O abundance is $<10^{-5}$, indicating that the absence of H_2O is not simply due to a lower envelope mass, but is likely caused by photodissociation of H_2O to OH in the more diffuse, lower-density Class I envelopes. Also, the longer timescale can result in H_2O freeze-out onto grain mantles after $\sim 10^5$ years (Bergin et al. 1998).

Two scenarios have been put forward for the origin of the molecular emission from Class 0 objects. Ceccarelli et al. (1999, 2000) and Maret et al. (2002) favor a model of a collapsing envelope in which the lower-lying lines originate from the outer envelope and the higher-lying lines from the inner hot core where ices evaporate (see Figure 6). In contrast, Giannini et al. (2001), Benedettini et al. (2002), and Nisini et al. (2000, 2002) argued that most of the emission arises in the J- and C-shocks associated with the outflow impacting the envelope, similar to what was discussed in Section 8. Arguments in favor of the latter explanation include (*a*) the fact that in some cases the lines have similar strengths at the source and off-source outflow positions, (*b*) the broad $\sim$20 km s^{-1} H_2O line profiles seen by *SWAS*, and (*c*) the linear relation between total line luminosity and the kinetic luminosity of the outflow derived from mapping of CO millimeter lines. The correlation with other molecular shock tracers such as SiO is less clear.

It should be kept in mind, however, that the observed amount of warm gas is typically only 0.01 $M_\odot$ (a few percent of the total envelope mass) and that evidence for warm inner envelopes and ice evaporation is clearly established from other data (see van Dishoeck 2003 for review). Larsson et al. (2002) argue that such models cannot reproduce the CO emission for one source, but the case for H_2O is less clear. For example, Maret et al. (2002) showed that for NGC 1333 IRAS4—a source where the molecular emission peaks at the YSO—the H_2O lines can be well explained with an abundance of 5×10^{-7} in the outer region and 5×10^{-6} in the inner envelope. For high-mass YSOs, ice evaporation contributes to the *SWAS* and *ISO* H_2O observations (see Sections 3.4 and 9.2). Finally, Ceccarelli et al. (2002b) suggested that some of the high-excitation CO may originate from a superheated disk in the embedded phase. Future high-spectral and -spatial data from the *Herschel Space Observatory* are needed to determine the relative contributions from each of these scenarios for a large sample of sources.

9.1.2. CAM-CVF AND SWS SURVEYS As noted in Section 4.2, CAM-CVF observations, together with a few SWS spectra, reveal the presence of abundant ices in the cold outer envelope of low-mass YSOs. However, the lack of spectral resolution prevents the establishment of any trends based on changing line profiles or gas/solid ratios, such as observed for high-mass YSOs. Medium resolution mid-IR spectroscopy of low-mass YSOs is an area that is wide open for future studies.

9.1.3. T TAU A special case is formed by T Tau, the prototypical Class II object but whose IR line spectra are more characteristic of an embedded Class I object. Indeed, T Tau has one of the richest SWS (van den Ancker et al. 1999) and LWS (Spinoglio et al. 2000) spectra, full of atomic and molecular (H_2, CO, H_2O, and OH) lines. In addition to shocks, the influence of UV radiation is clearly seen in the fluorescent H_2 component and in the H_2O–OH chemistry. T Tau may be peculiar because it is a close binary system with a dusty envelope seen face-on, filling a large fraction of the beam.

9.1.4. FU ORIONIS OBJECTS Another interesting sample is formed by the FU Orionis objects, studied with the LWS by Lorenzetti et al. (2000). These are low-luminosity young stars that show a sudden increase in brightness thought to be caused by a large increase in the disk accretion rate. In addition to the usual atomic [O I] and [C II] fine-structure lines, these objects surprisingly show [N II] 122 μm emission, not seen toward any other type of YSO. [N II] must arise from ionized gas, and because no higher ionization stages of other elements are seen, this gas must have a low ionization fraction and low density ($n(e) \lesssim 100$ cm^{-3}). One possibility is that it is produced by enhanced UV radiation from the disk-star boundary layer.

9.2. Intermediate and High-Mass YSOs

Several samples of intermediate- and high-mass sources have been studied with *ISO*, for different purposes. Lorenzetti et al. (2002) summarize the LWS observations on Herbig Ae/Be stars, covering luminosities from 5 to 10^5 $L_\odot$ (see also Giannini et al. 1999, Lorenzetti et al. 1999). Most of these objects are associated with diffuse nebulosity and show [C II] and [O I] fine-structure emission characteristic of PDRs. Some of the extended PAH emission has been imaged by

Siebenmorgen et al. (2000). High-luminosity ($>10^4$ $L_\odot$) deeply embedded sources studied with the SWS are summarized by Gibb et al. (2004), whereas a catalogue of SWS-LWS spectra of H II regions is presented by Peeters et al. (2002b). LWS spectra of other high-luminosity objects are summarized by Benedettini et al. (2003). A common characteristic of all these luminous sources is that they show almost no molecular emission lines, and often just a handful of atomic emission lines, usually only [O I] 63 μm and [C II] 158 μm arising in a PDR component. If an H II region has started to develop, higher-ionization stages are seen as well and can be used to determine the effective temperature and spectral type of the embedded source. Molecular material, both in the gas and solid state, is however present and is prominently seen in SWS absorption spectra.

9.2.1. FROM SHOCKS TO PDRs Two particularly illustrative examples of the combined SWS and LWS spectral evolution have been provided by van den Ancker et al. (2000b,c). The first concerns the BD + 40°4124 group containing three YSOs with IR luminosities of 270–1600 $L_\odot$ (see Figure 17). The LkHα 225 spectrum is characteristic of a deeply embedded source, with deep silicate and ice absorptions. LkHα 224 is an example of a new class of nearly featureless sources, showing no silicate or ice absorption or emission. The spectrum of BD + 40°4124 itself, a B2Ve star, has strong PAHs and many atomic lines. Van den Ancker et al. (2000c) show that the atomic and H_2 lines for the embedded sources originate from shocks, whereas those for BD + 40°4124 are characteristic of a PDR, with a contribution from the H II region. Thus, as the envelope disperses, the PDR component starts to dominate compared with the shock emission.

A similar picture is found from comparing two high-luminosity ($2-4\times10^4$ $L_\odot$) objects, Cep A and S 106 (van den Ancker et al. 2000b). The Cep A spectrum shows deep ice and silicate absorptions, but no PAH emission nor ionized atomic lines, indicating that it has not yet started to develop its H II region. In contrast, the S 106 spectrum is dominated by PAHs and by atomic lines from a wide range of ionization stages characteristic of a young O8 star. The atomic and molecular H_2 and CO emission lines indicate shock excitation for Cep A and PDR excitation for S 106. The situation for other high-mass YSOs is often less clear-cut. For example, the Orion SWS spectra reveal a mixture of many physical components in the beam, including the foreground H II region, the PDR, the powerful outflow, and the embedded YSO (van Dishoeck et al. 1998).

9.2.2. EVOLUTION WITHIN THE DEEPLY EMBEDDED STAGE Whereas the above characteristics of the deeply embedded versus the more evolved PDR/H II region stages are readily recognized, more subtle evolutionary effects within the deeply embedded stage can be derived from careful analysis of the ice and gas-phase absorption data toward high-mass protostars. These are very young objects, before the onset of the ultracompact H II region or hot core stage. As discussed in Section 4.3, the profiles of several ice bands show strong evidence of progressive heating of the envelope. Similarly, the gas/solid ratios of species like H_2O

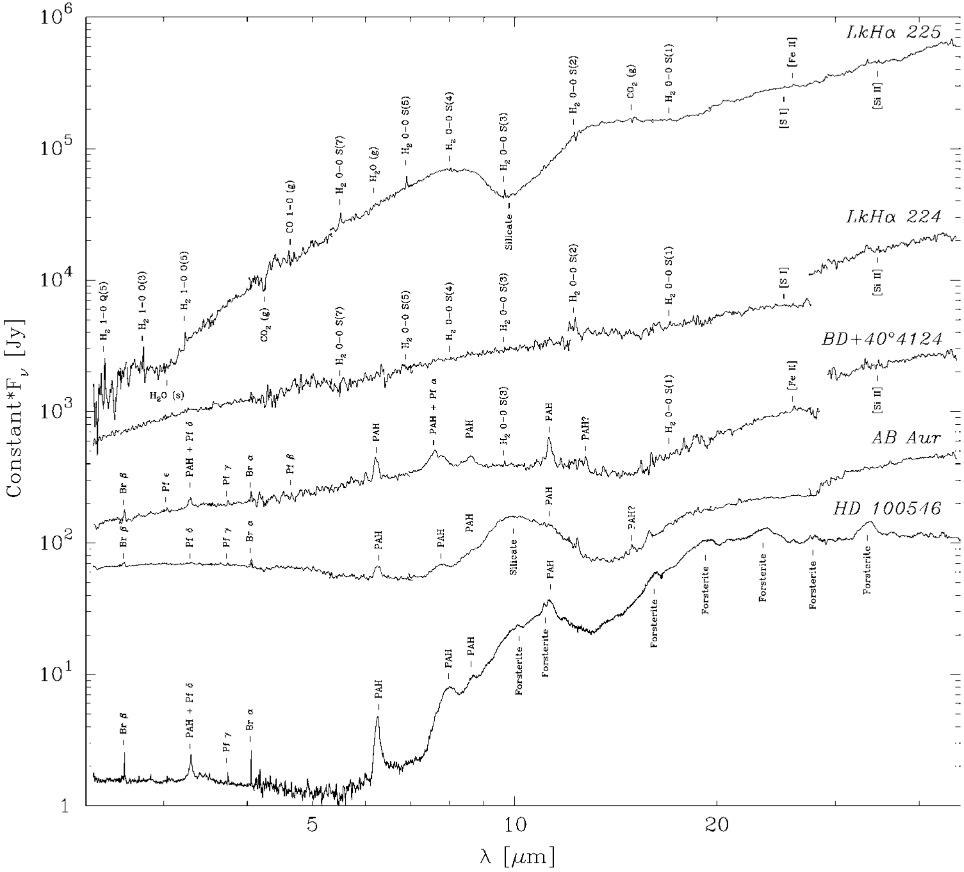

Figure 17 SWS spectra of young stars at different stages of evolution (van den Ancker et al. 2000a,c; Malfait et al. 1998). From top to bottom—in a rough evolutionary sequence—the spectra change from dominated by solid-state absorption features and gas (shock) emission lines, to PAH features and PDR lines, to amorphous and crystalline silicates.

increase systematically for the same sources, as does the color temperature of the cold dust. The most likely scenario, put forward by van der Tak et al. (2000b), is that the warmer sources have a lower ratio of envelope mass $M_{\rm env}$ compared with the bolometric luminosity of the source $L_{\rm bol}$, so that the overall temperatures are higher. If the lower $M_{\rm env}$ are due to the gradual dispersion of the envelope rather than to initial conditions, the sources can be put in a time sequence with the warmer sources being more evolved, thus providing a powerful diagnostic of the first few $\times 10^4$ years of protostellar evolution.

Why do high-mass sources not show more prominent molecular emission lines in the SWS and LWS spectra, like their low-mass counterparts? The main reason must be beam dilution, because the high-mass sources often have ten times larger distances. Detailed modeling shows that the hot core region where the temperature is above that for ice evaporation of 90 K is typically 1000 AU, less than $1''$ at >1 kpc. Apparently, shocks have an equally low filling factor, as evidenced from the absence of H_2 or [S I] emission lines. Moreover, the far-IR continuum of high-mass YSOs is so strong that weak emission lines are more difficult to detect at low spectral resolution.

The case of H_2O is instructive of the abundance and excitation variations within high-mass envelopes. Boonman et al. (2003a) analyzed all available H_2O SWS, LWS, and *SWAS* data in terms of possible abundance profiles. The SWS data indicate ice evaporation in the inner hot core with abundances of $>10^{-4}$, whereas the absence of LWS lines and the weak *SWAS* emission require significant H_2O freeze-out in the outer cold envelope with abundances $<10^{-8}$ at $T < 90$ K (see also Snell et al. 2000). The *SWAS* profiles consist of narrow and broad components, with the outflow contribution at most 50%. In some cases, only a narrow (<few km s^{-1}) profile is seen with a line strength consistent with optically thick H_2O emission at $\sim$100 K arising from a $\sim 1''$ source. This emphasizes the need for future high spatial and spectral resolution H_2O observations to properly disentangle the shock, envelope and hot core components.

10. CIRCUMSTELLAR DISKS AROUND YOUNG STARS

10.1. Dust Evolution and Disk Structure

As discussed in Sections 5 and 6, the mid- and far-IR spectra of disks around young stars exhibit a wide variety of features owing to crystalline silicates, PAHs, and ices (Meeus et al. 2001, Bouwman et al. 2001). Although no trend with age within the pre-main sequence stage has been found, there are clear indications that the dust evolves from the diffuse cloud to the disk phase. Analysis of the 10 μm silicate band shows two effects. The first is coagulation of 0.1 μm to micron-sized grains. Interestingly, small PAHs remain present during this process, although their spectral characteristics are clearly different from those of molecular clouds (Peeters et al. 2002a). The second effect is crystallization, resulting in an increasing fraction of emission from forsterite and other minerals when going from the Herbig Ae stars to a debris disk like β Pictoris and comets like Halley and Hale-Bopp (Figure 12). The near-complete absence of crystalline silicates in interstellar clouds indicates that the crystallization must occur in the disks themselves. The correlation of forsterite with silica suggests that thermal annealing is the dominant process, but this has to occur at temperatures greater than ~1100 K for the timescale to be shorter than the disk lifetime. Because the crystalline material is observed at lower temperatures further out in the disk, this implies that some radial mixing process must occur (see also Bockelée-Morvan et al. 2002), although the mechanisms are not yet well understood. The data indicate that the timescale for annealing is longer than that of coagulation. The origin of crystalline water in cold disks like that around HD 142527 (Figure 11) is also unclear.

The mid-IR spectra, combined with their SEDs, also provide insight into the physical structure of disks. Natta et al. (2000) noted that the silicate emission seen in the PHOT-S spectra of T Tauri stars requires the presence of a disk atmosphere, in which the disk surface is heated from the top by radiation from the star (Calvet et al. 1992, Chiang & Goldreich 1997, Chiang et al. 2001). Meeus et al. (2001) divided the isolated Herbig Ae star *ISO* spectra into two groups: those with a rising SED (Group I) and those with a flat continuum (Group II). The SEDs of the latter group can be fitted with a power-law provided by an optically thick but geometrically thin disk, whereas the former requires addition of a black-body component with 100–200 K provided by a disk atmosphere in the inner ~10 AU (see Figure 10).

Natta et al. (2001) and Dullemond et al. (2001) (see also Dominik et al. 2003) propose a slight modification, in which the inner disk is truncated at the dust sublimation temperature of ~1400 K at ~0.5 AU, resulting in a sharp rim exposed to intense radiation and producing most of the near-IR radiation. Owing to the higher temperatures, the rim has an increased scale height (puffed up), shielding the outer parts of the disk and resulting in lower temperatures in shadowed regions. Group I sources have a flaring outer disk directly exposed to the stellar radiation, where the silicate and PAH emission is thought to arise. In Group II sources, the disk may be so small that there is no flaring region. Alternatively, grain growth and/or dust settling may cause the disk to become self-shadowing (Dullemond & Dominik 2004). The precise origin of the silicate emission in Group II sources is not yet fully understood. The presence of an additional spherical (remnant) envelope cannot be excluded for some cases (e.g., Miroshnichenko et al. 1999), and spatially resolved data are essential to disentangle the different components.

The disk around HD 100546 is clearly different from that around other stars: Nearly 70% of the absorbed and re-emitted starlight of HD 100546 emerges at mid- rather than near-IR wavelengths, indicating that the disk must intercept the radiation at larger distances, around 10 AU. Another peculiarity of this object is that the crystalline silicates have a lower temperature than the amorphous material and an increasing abundance with radial distance. One possibility is that a proto-Jovian planet has cleared out a gap around 10 AU, leading to a puffed up rim on the far side of the gap (Bouwman et al. 2003). The wealth of crystalline silicates could have been produced in a collisional cascade of asteroidal-sized objects stirred up by the proto-Jupiter, or by shocks caused by tidal interactions of the planet with the disk producing crystalline material through flash heating. Some of this material could have been lifted and scattered to the disk surface and driven out by radiation pressure to larger distances. High spatial resolution data are needed to confirm this scenario, but it illustrates the potential of mid-IR spectroscopy to trace planet-formation processes.

The similarity of the HD 100546 and comet Hale-Bopp spectra (Crovisier et al. 1997) has often been cited as evidence of a strong interstellar medium-solar system connection, although the scenario described above is quite specific for one object. Additional evidence for such a connection has been derived from the fact that the ice abundances found in protostellar regions (see Section 4.2) are comparable to those observed in cometary comae (e.g., Ehrenfreund et al. 1997b, Bockelée-Morvan et al. 2000). This ice similarity is strong evidence that some fraction of the interstellar material must have been included largely unaltered, but the origin of the crystalline silicates in comets is still a mystery in this context.

10.2. Gas in Disks

An equally important issue is the timescale over which the gas disappears from the disk because this directly affects the formation of gaseous giant planets. Ground-based millimeter CO surveys are hampered by freeze-out in the cold parts of the disk and photodissociation in the upper layers (e.g., Aikawa et al. 2002), whereas IR CO lines probe only a small fraction of warm gas (e.g., Najita et al. 2003). The lowest H_2 pure-rotational lines provide a powerful alternative gas probe because it is the dominant constituent of the gas, does not freeze-out onto grains, self-shields effectively against photodissociation, and has optically thin lines. The main disadvantage is that the pure rotational lines are intrinsically weak and difficult to detect superposed on a strong continuum at low spectral resolution. Also, the gas temperature needs to be sufficiently high, >80 K.

Deep searches for the H_2 S(0) and S(1) lines at 28 and 17 μm have been performed with the SWS toward a dozen young stars (Thi et al. 2001a,b). These sources were chosen to be isolated objects to minimize contamination from surrounding cloud material. Detections of lines have been claimed in several sources, including potentially some older Vega-type objects, but confirmation with higher spatial- and spectral-resolution data is needed (see Richter et al. 2002). Because the mid-IR H_2 lines are sensitive to a fraction of $M_{\rm Jup}$ of warm gas, they are well worth pursuing with future instrumentation. Other gas tracers such as the [C II] 157.7 μm line have been considered as well (Kamp et al. 2003).

11. CONCLUDING REMARKS

ISO has clearly demonstrated the power of full mid- and far-IR spectra to probe a wide variety of processes associated with star and planet formation, providing insight that cannot be obtained from imaging data alone. Using *ISO*, researchers have completed the inventory of ices, obtained a census of the PAHs features, opened up a new diagnostic of warm gas (H_2), widely observed key gas-phase molecules (H_2O, CO_2), and revealed a wealth of crystalline silicate features. More importantly, *ISO* has shown systematic variations in the features during the star-formation process, providing a spectral classification scheme of the earliest embedded stages that are difficult to probe otherwise and stimulating new models. Related variations in the composition of the material when it is cycled from one phase to another are also found: freeze-out and evaporation of ices, ionization and rehydrogenation of PAHs, and amorphization, crystallization, and coagulation of silicates. At all stages, specific lines and line ratios provide powerful diagnostics of temperatures and densities, as well as the relative importance of shock and photon heating of the gas. Because many of these same features and processes are also ubiquitous in extragalactic sources out to the highest redshifts, a good understanding of their diagnostic capabilities locally is essential. The *ISO* archive will remain a valuable—and in many ways unique—resource for future studies.

At the time of writing, the first results from the *Spitzer Space Telescope* are just emerging. With its increased sensitivity up to two orders of magnitude, Spitzer will extend mid- and far-IR imaging and spectroscopy into new regimes that *ISO* could not probe, such as medium resolution spectroscopy of embedded low-mass protostars, of disks around young stars down to the brown-dwarf regime, of debris disks, and of H_2 and other lines in the most diffuse PDRs and weakest shocks. The *ISO* spectra summarized here form a guideline to the interpretation of the Spitzer data. Spitzer's spectroscopic capabilities are limited, however, both in spectral resolution and wavelength coverage. A combination of several future missions, in particular the *Stratospheric Observatory for Infrared Astronomy* (SOFIA), ASTRO-F, the *Herschel Space Observatory*, and the *James Webb Space Telescope* (*JWST*), are needed to obtain spectra over the full 2.4–200 μm range covered by *ISO*. The highest spectral and spatial resolution data will be provided at mid-IR wavelengths by large optical ground-based telescopes, and at submillimeter wavelengths by the Atacama Large Millimeter Array (ALMA) and other millimeter arrays. *ISO* has paved the way for the exciting science to be performed with these new facilities.

ACKNOWLEDGMENTS

The spectra presented here are a testimony to the ingenuity of the instrument builders and their teams, both hardware and software. I am grateful to many colleagues for communicating results and figures prior to publication and for countless stimulating discussions, making *ISO* such a fun project. The writing of this review was supported by a Spinoza grant from the Netherlands Organization for Scientific Research (NWO) and by the Moore's Scholar Program of the California Institute of Technology.

The *Annual Review of Astronomy and Astrophysics* is online at http://astro.annualreviews.org

LITERATURE CITED

Aannestad PA, Emery RJ. 2001. *Astron. Astrophys.* 376:1040–53

Aannestad PA, Emery RJ. 2003. *Astron. Astrophys.* 406:155–64

Abergel A, Bernard JP, Boulanger F, Cesarsky C, Desert FX, et al. 1996. *Astron. Astrophys.* 315:L329–33

Abergel A, Bernard JP, Boulanger F, Cesarsky D, Falgarone E, et al. 2002. *Astron. Astrophys.* 389:239–51

Abergel A, Teyssier D, Bernard JP, Boulanger F, Coulais A, et al. 2003. *Astron. Astrophys.* 410:577–85

Aikawa Y, van Zadelhoff GJ, van Dishoeck EF, Herbst E. 2002. *Astron. Astrophys.* 386:622–32

Alexander RD, Casali MM, André P, Persi P, Eiroa C. 2003. *Astron. Astrophys.* 401:613–24

Allamandola LJ, Hudgins DM, Sandford SA. 1999. *Ap. J. Lett.* 511:L115–19

Allamandola LJ, Tielens AGGM, Barker JR. 1985. *Ap. J.* 290:L25–28

André P, Ward-Thompson D, Barsony M. 2000. In *Protostars and Planets IV*, ed. V Mannings, AP Boss, SS Russell, pp. 59–96. Tucson: Univ. Ariz.

Bacmann A, André P, Puget JL, Abergel A, Bontemps S, Ward-Thomson D. 2000. *Astron. Astrophys.* 361:555–80

Bakes ELO, Tielens AGGM. 1994. *Ap. J.* 427:822–38

Bakes ELO, Tielens AGGM, Bauschlicher CW. 2001. *Ap. J.* 556:501–14

Baluteau JP, Cox P, Cernicharo J, Péquinot D, Caux E, et al. 1997. *Astron. Astrophys.* 322:L33–36

Benedettini M, Pezzuto S, Spinoglio L, Saraceno P, Di Giorgio AM. 2003. In *Recent Research Development in Astronomy and Astrophysics*, ed. Res. Signpost, pp. 591–607 (astro-ph/0310086)

Benedettini M, Viti S, Giannini T, Nisini B, Goldsmith PF, Saraceno P. 2002. *Astron. Astrophys.* 395:657–62

Bergin EA, Kaufman MJ, Melnick GJ, Snell RL, Howe JE. 2003. *Ap. J.* 582:830–45

Bergin EA, Neufeld DA, Melnick GJ. 1998. *Ap. J.* 499:777–92

Bertoldi F. 1997. See Heras et al. 1997, pp. 67–72

Bertoldi F, Timmermann R, Rosenthal D, Drapatz S, Wright CM. 1999. *Astron. Astrophys.* 346:267–77

Black JH, van Dishoeck EF. 1987. *Ap. J.* 322:412–49

Bockelée-Morvan D, Gautier D, Hersant F, Huré JM, Robert F. 2002. *Astron. Astrophys.* 384:1107–18

Bockelée-Morvan D, Lis DC, Wink JE, Despois D, Crovisier J, et al. 2000. *Astron. Astrophys.* 353:1101–14

Boogert ACA, Ehrenfreund P. 2004. In *The Astrophysics of Dust*, ed. AN Witt, GC Clayton, BT Draine. San Francisco: ASP. In press

Boogert ACA, Ehrenfreund P, Gerakines P, Tielens AGGM, Whittet DCB, et al. 2000a. *Astron. Astrophys.* 353:349–62

Boogert ACA, Helmich FP, van Dishoeck EF, Schutte WA, Tielens AGGM, Whittet DCB. 1998. *Astron. Astrophys.* 336:352–58

Boogert ACA, Hogerheijde MR, Ceccarelli C, Tielens AGGM, van Dishoeck EF, et al. 2002. *Ap. J.* 570:708–23

Boogert ACA, Tielens AGGM, Ceccarelli C, Boonman AMS, van Dishoeck EF, et al. 2000b. *Astron. Astrophys.* 360:683–98

Boonman AMS, Doty SD, van Dishoeck EF, Bergin EA, Melnick GJ, et al. 2003a. *Astron. Astrophys.* 406:937–55

Boonman AMS, Stark R, van der Tak FFS, van Dishoeck EF, van der Wal PB, et al. 2001. *Ap. J. Lett.* 553:L63–66

Boonman AMS, van Dishoeck EF. 2003c. *Astron. Astrophys.* 403:1003–10

Boonman AMS, van Dishoeck EF, Lahuis F, Doty SD. 2003b. *Astron. Astrophys.* 399:1063–72

Boonman AMS, van Dishoeck EF, Lahuis F, Doty SD, Wright CM, Rosenthal D. 2003c. *Astron. Astrophys.* 399:1047–61

Boudin N, Schutte WA, Greenberg JM. 1998. *Astron. Astrophys.* 331:749–59

Boulanger F, Abergel A, Cesarsky D, Bernard JP, Miville-Deschênes MA, et al. 2000. In *ISO Beyond Point Sources: Studies of Extended Infrared Emission*, ed. RJ Laureijs, K Leech, MF Kessler, ESA SP-455, p. 91

Boulanger F, Boissel P, Cesarsky D, Ryter C. 1998. *Astron. Astrophys.* 339:194–200

Boulanger F, Falgarone E, Puget JL, Helou G. 1990. *Ap. J.* 364:136–45

Bouwman J, de Koter A, Dominik C, Waters LBFM. 2003. *Astron. Astrophys.* 401:577–92

Bouwman J, de Koter A, van den Ancker ME, Waters LBFM. 2000. *Astron. Astrophys.* 360:213–26

Bouwman J, Meeus G, de Koter A, Hony S, Dominik C, Waters LBFM. 2001. *Astron. Astrophys.* 375:950–62

Bowey JE, Adamson AJ. 2002. *MNRAS* 334:94–106

Brooks KJ, Cox P, Schneider N, Storey JWV, Poglitsch A, et al. 2003. *Astron. Astrophys.* 412:751–65

Cabrit S, Bontemps S, Lagage PO, Sauvage M, Boulanger F, et al. 1999. See Cox & Kessler 1999, pp. 449–52

Cabrit S, Lefloch B, Cernicharo J, Pineau des Forêts G, Le Bourlot J, Flower D. 2004. In *The Dense Interstellar Medium in Galaxies*, ed. S Pfalzner, C Kramer, C Straubmeier, A Heithausen. pp. 587–92. Berlin: Springer-Verlag

Calvet N, Magris GC, Patino A, d'Alessio P. 1992. *Rev. Mex. Astron. Astrofis.* 24:27–42

Caux E, Ceccarelli C, Castets A, Vastel C, Liseau R, et al. 1999. *Astron. Astrophys.* 347:L1–4

Caux E, Ceccarelli C, Pagani L, Maret S, Castets A, Pardo JR. 2002. *Astron. Astrophys.* 383:L9–13

Cazaux S, Tielens AGGM. 2002. *Ap. J. Lett.* 577:L29–32

Ceccarelli C, Baluteau JP, Walmsley M, Swinyard BM, Caux E, et al. 2002a. *Astron. Astrophys.* 383:603–13

Ceccarelli C, Boogert ACA, Tielens AGGM, Caux E, Hogerheijde MR, Parise B. 2002b. *Astron. Astrophys.* 395:863–71

Ceccarelli C, Castets A, Caux D, Loinard L, Molinari S, Tielens AGGM. 2000. *Astron. Astrophys.* 355:1129–37

Ceccarelli C, Caux E, Loinard L, Castets A, Tielens AGGM, et al. 1999. *Astron. Astrophys.* 342: L21–24

Ceccarelli C, Caux E, Tielens AGGM, Kemper F, Waters LBFM, Phillips T. 2002c. *Astron. Astrophys.* 395:L29–33

Ceccarelli C, Caux E, White GJ, Molinari S, Furniss I, et al. 1998a. *Astron. Astrophys.* 331:372–82

Ceccarelli C, Caux E, Wolfire M, Rudolph A, Nisini B, et al. 1998b. *Astron. Astrophys.* 331:L17–20

Cernicharo J, Goicoechea JR, Benilan Y. 2002. *Ap. J. Lett.* 580:L157–60

Cernicharo J, Goicoechea JR, Caux E. 2000a. *Ap. J. Lett.* 534:L199–102

Cernicharo J, Heras AM, Pardo JR, Tielens AGGM, Guélin M, et al. 2001b. *Ap. J. Lett.* 546:L127–30

Cernicharo J, Heras AM, Tielens AGGM, Pardo JR, Herpin F, et al. 2001a. *Ap. J. Lett.* 546:L123–26

Cernicharo J, Lim T, Cox P, González-Alfonso E, Caux E, et al. 1997. *Astron. Astrophys.* 323:L25–28

Cernicharo J, Noriega-Crespo A, Cesarsky D, Lefloch B, González-Alfonso E, et al. 2000b. *Science* 288:649–52

Cesarsky C, Abergel A, Agnèse P, Altieri B, Augueres JL, et al. 1996. *Astron. Astrophys.* 315:L32–37

Cesarsky D, Cox P, Pineau des Forêts G, van Dishoeck EF, Boulanger F, Wright CM. 1999. *Astron. Astrophys.* 348:945–49

Cesarsky D, Jones AP, Lequeux J, Verstraete L. 2000a. *Astron. Astrophys.* 358:708–16

Cesarsky D, Lequeux J, Ryter C, Gérin M. 2000b. *Astron. Astrophys.* 354:L87–91

Chiang EI, Goldreich P. 1997. *Ap. J.* 490:368–76

Chiang EI, Joung MK, Creech-Eakman MJ, Qi C, Kessler JE, et al. 2001. *Ap. J.* 547:1077–89

Chiar JE, Tielens AGGM, Whittet DCB, Schutte WA, Boogert ACA, et al. 2000. *Ap. J.* 537:749–62

Chièze JP, Pineau des Forêts G, Flower DR. 1998. *MNRAS* 295:672–82

Churchwell E. 2002. *Annu. Rev. Astron. Astrophys.* 40:27–62

Clegg PE, Ade PAR, Armand C, Baluteau JP, Barlow MJ, et al. 1996. *Astron. Astrophys.* 315:L38–42

Cox P, Kessler MF. 1999. *The Universe as Seen by ISO*. ESA SP-427. Noordwijk: ESTEC. 1090 pp.

Creech-Eakman MJ, Chiang EI, Joung RMK, Blake GA, van Dishoeck EF. 2002. *Astron. Astrophys.* 385:546–62

Crovisier J, Leech K, Bockelée-Morvan D, Brooke TY, Hanner MS, et al. 1997. *Science* 275:1904–7

Dartois E, Cox P, Roelfsema PR, Jones AP, Tielens AGGM, et al. 1998a. *Astron. Astrophys.* 338:L21–24

Dartois E, Demyk K, d'Hendecourt L, Ehrenfreund P. 1999. *Astron. Astrophys.* 351:1066–74

Dartois E, d'Hendecourt L. 2001. *Astron. Astrophys.* 365:144–56

Dartois E, d'Hendecourt L, Boulanger F, Jourdain de Muizon M, Breitfellner M, et al. 1998b. *Astron. Astrophys.* 331:651–60

Dartois E, Thi WF, Geballe TR, Deboffle D, d'Hendecourt L, van Dishoeck E. 2003. *Astron. Astrophys.* 399:1009–20

de Graauw Th, Haser LN, Beintema DA, Roelfsema PR, van Agthoven H, et al. 1996a. *Astron. Astrophys.* 315:L49–54

de Graauw Th, Whittet DCB, Gerakines PA, Bauer O, Beintema DA, et al. 1996b. *Astron. Astrophys.* 315:L345–48

Demyk K, Dartois E, d'Hendecourt L, Jourdain de Muizon M, Heras AM, Breitfellner M. 1998. *Astron. Astrophys.* 339:553–60

Demyk K, Jones AP, Dartois E, Cox P, d'Hendecourt L. 1999. *Astron. Astrophys.* 349:267–75

d'Hendecourt L, Joblin C, Jones A, eds. 1999. *Solid Interstellar Matter: The ISO Revolution*. Berlin: Springer-Verlag. 315 pp.

Dominik C, Dullemond CP, Waters LBFM, Walch S. 2003. *Astron. Astrophys.* 398:607–19

Draine BT. 1978. *Ap. J. Suppl.* 36:595–619

Draine BT. 2003. *Annu. Rev. Astron. Astrophys.* 41:241–89

Draine BT, Bertoldi F. 1996. *Ap. J.* 468:269–89

Draine BT, Bertoldi F. 1999. See Cox & Kessler 1999, pp. 353–59

Draine BT, McKee CF. 1993. *Annu. Rev. Astron. Astrophys.* 31:373–432

Duley WW. 1996. *MNRAS* 279:591–94

Duley WW, Williams DA. 1981. *MNRAS* 196:269–74

Dullemond CP, Dominik C. 2004. *Astron. Astrophys.* 417:159–68

Dullemond CP, Dominik C, Natta A. 2001. *Ap. J.* 560:957–69

Ehrenfreund P, Boogert ACA, Gerakines PA, Jansen DJ, Schutte WA, et al. 1996. *Astron. Astrophys.* 315:L341–44

Ehrenfreund P, Boogert ACA, Gerakines PA, Tielens AGGM, van Dishoeck EF. 1999a. *Astron. Astrophys.* 328:649–69

Ehrenfreund P, Dartois E, Demyk K, d'Hendecourt L. 1998. *Astron. Astrophys.* 339:L17–20

Ehrenfreund P, d'Hendecourt L, Dartois E, Jourdain de Muizon M, Breitfellner M, et al. 1997b. *Icarus* 130:1–15

Ehrenfreund P, Schutte WA. 2000. In *IAU Symp. 197, Astrochemistry*, ed. YC Minh, EF van Dishoeck, pp. 135–46. San Francisco: Astron. Soc. Pac.

Evans NJ, Lacy JH, Carr JS. 1991. *Ap. J.* 383:674–92

Feldt M, Henning Th, Lagage PO, Manske V, Schreyer K, Stecklum B. 1998. *Astron. Astrophys.* 332:849–56

Feuchtgruber H, Helmich FP, van Dishoeck EF, Wright CM. 2000. *Ap. J. Lett.* 535:L111–14

Froebrich D, Smith MD, Eislöffel J. 2002. *Astron. Astrophys.* 385:239–56

Fuente A, Martín-Pintado J, Rodríguez-Fernández NJ, Cernicharo J, Gerin M. 2000. *Astron. Astrophys.* 354:1053–61

Fuente A, Martín-Pintado J, Rodríguez-Fernández NJ, Rodríguez-Franco A, de Vicente P, Kunze D. 1999. *Ap. J. Lett.* 518:L45–48

Genzel R, Cesarsky C. 2000. *Annu. Rev. Astron. Astrophys.* 38:761–814

Gerakines PA, Schutte WA, Ehrenfreund P. 1996. *Astron. Astrophys.* 312:289–305

Gerakines PA, Schutte WA, Greenberg JM, van Dishoeck EF. 1995. *Astron. Astrophys.* 296:810–18

Gerakines PA, Whittet DCB, Ehrenfreund P, Boogert ACA, Tielens AGGM, et al. 1999. *Ap. J.* 522:357–77

Giannini T, Lorenzetti D, Tommasi E, Nisini B, Benedettini M, et al. 1999. *Astron. Astrophys.* 346:617–25

Giannini T, Nisini B, Lorenzetti D. 2001. *Ap. J.* 555:40–57

Giannini T, Nisini B, Lorenzetti D, Di Giorgio AM, Spinoglio L, et al. 2000. *Astron. Astrophys.* 358:310–20

Gibb EL, Whittet DCB. 2002. *Ap. J. Lett.* 566:L113–16

Gibb EL, Whittet DCB, Boogert ACA, Tielens AGGM. 2004. *Ap. J. Suppl.* 151:35–73

Gibb EL, Whittet DCB, Schutte WA, Boogert ACA, Chair JE, et al. 2000. *Ap. J.* 536:347–56

Gillett FC, Forrest WJ. 1973. *Ap. J.* 179:483–91

Goicoechea JR, Cernicharo J. 2000a. *Ap. J. Lett.* 554:L213–16

Goicoechea JR, Cernicharo J. 2000b. In *The Promise of the Herschel Space Observatory*, ed. GL Pilbratt, J Cernicharo, AM Heras, T Prusti, R Harris, et al. ESA SP-460, pp. 413–16. Noordwijk: ESTEC

Goicoechea JR, Cernicharo J. 2002. *Ap. J. Lett.* 576:L77–81

Goldsmith PF, Melnick GJ, Bergin EA, Howe JE, Snell RL, et al. 2000. *Ap. J. Lett.* 539:L123–27

González-Alfonso E, Cernicharo J, van Dishoeck EF, Wright CM, Heras A. 1998. *Ap. J. Lett.* 502:L169–72

González-Alfonso E, Wright CM, Cernicharo J, Rosenthal D, Boonman AMS, van Dishoeck EF. 2002. *Astron. Astrophys.* 386:1074–1102

Greenberg JM, Li A, Mendoza-Gomez CX, Schutte WA, Gerakines PA, de Groot M. 1995. *Ap. J. Lett.* 455:L177–80

Gry C, Boulanger F, Nehmé C, Pineau des Forêts G, Habart E, Falgarone E. 2002. *Astron. Astrophys.* 391:675–80

Gürtler J, Henning Th, Kömpe C, Pfau W, Krätschmer W, Lemke D. 1996. *Astron. Astrophys.* 315:L189–92

Gürtler J, Klaas U, Henning Th, Ábrahám P, Lemke D, et al. 2002. *Astron. Astrophys.* 390:1075–87

Gürtler J, Schreyer K, Henning Th, Lemke D, Pfau W. 1999. *Astron. Astrophys.* 346:205–10

Haas MR, Davidson JA, Erickson EF, eds. 1995. *Airborne Astronomy Symp. Galactic Ecosystem: From Gas to Stars to Dust* Vol. 73. San Francisco: ASP. 737 pp.

Habart E, Boulanger F, Verstraete L, Pineau des Forêts G, Falgarone E, Abergel A. 2003. *Astron. Astrophys.* 397:623–34

Habart E, Verstraete L, Boulanger F, Pineau des Forêts G, Le Peintre F, Bernard JP. 2001. *Astron. Astrophys.* 373:702–13

Habart E, Boulanger F, Verstraete L, Walmsley CM, Pineau des Forêts G. 2004. *Astron. Astrophys.* 414:531–44

Habing HJ. 1968. *Bull. Astron. Neth.* 19:421–32

Harwit M, Neufeld DA, Melnick GJ, Kaufman MJ. 1998. *Ap. J. Lett.* 497:L105–8

Helmich FP, van Dishoeck EF, Black JH, de Graauw T, Beintema DA, et al. 1996. *Astron. Astrophys.* 315:L173–76

Henning Th, ed. 2003. *Astromineralogy*. Berlin: Springer-Verlag. 281 pp.

Heras AM, Leech K, Trams NR, Perry M, eds. 1997. *1st ISO Workshop Analyt. Spectrosc.*, ESA SP-419. Noordwijk: ESA-ESTEC. 319 pp.

Hollenbach D. 1997. See Reipurth & Bertout 1997, pp. 182–98

Hollenbach D, Chernoff DF, McKee CF. 1989. In *Infrared Spectroscopy in Astronomy*, ESA SP-290, pp. 245–58. Noordwijk: ESTEC

Hollenbach D, Salpeter EE. 1971. *Ap. J.* 163:155–64

Hollenbach DJ, Tielens AGGM. 1997. *Annu. Rev. Astron. Astrophys.* 35:179–216

Hollenbach DJ, Tielens AGGM. 1999. *Rev. Mod. Phys.* 71:173–230

Honda M, Kataza H, Okamoto YK, Miyata T, Yamashita T, et al. 2003. *Ap. J. Lett.* 585:L59–62

Hony S, van Kerckhoven C, Peeters E, Tielens AGGM, Hudgins DM, Allamandola LJ. 2001. *Astron. Astrophys.* 370:1030–43

Hudgins DM, Allamandola LJ. 1999. *Ap. J. Lett.* 516:L41–44

Hudgins DM, Sandford SA, Allamandola LJ, Tielens AGGM. 1993. *Ap. J. Suppl.* 86:713–870

Jones AP, Frey V, Verstraete L, Cox P, Demyk K. 1999. See Cox et al. 1999, pp. 679–82

Jura M. 1975. *Ap. J.* 197:575–80

Kahanpää J, Mattila K, Lehtinen K, Leinert C, Lemke D. 2003. *Astron. Astrophys.* 405:999–1012

Kamp I, van Zadelhoff GJ, van Dishoeck EF, Stark R. 2003. *Astron. Astrophys.* 397:1129–41

Kaufman MJ, Neufeld DA. 1996. *Ap. J.* 456:611–30

Kaufman MJ, Wolfire MG, Hollenbach DJ, Luhman ML. 1999. *Ap. J.* 527:795–813

Keane JV, Boonman AMS, Tielens AGGM, van Dishoeck EF. 2000a. *Astron. Astrophys.* 376:L5–8

Keane JV, Tielens AGGM, Boogert ACA, Schutte WA, Whittet DCB. 2000b. *Astron. Astrophys.* 376:254–70

Keller LP, Hony S, Bradley JP, Molster FJ, Waters LBFM et al. 2002. *Nature* 417:148–50

Kemper F, Jäger C, Waters LBFM, Henning Th, Molster FJ, et al. 2002. *Nature* 415:295–97

Kemper F, Spaans M, Jansen DJ, Hogerheijde MR, van Dishoeck EF, Tielens AGGM. 1999. *Ap. J.* 515:649–56

Kemper F, Vriend WJ, Tielens AGGM. 2004. *Ap. J.* In press

Kessler MF, Müller TG, Leech K, Arviset C, García-Lario P, et al. 2003. *ISO-Mission and Satellite Overview.* ESA SP-1262. Noordwijk: ESA-ESTEC. 352 pp.

Kessler MF, Steinz JA, Anderegg ME, Clavel J, Drechsel G, et al. 1996. *Astron. Astrophys.* 315:L27–31

Krause O, Lemke D, Tóth LV, Klaas U, Haas M, et al. 2003. *Astron. Astrophys.* 398:1007–20

Lada CJ. 1999. In *The Origin of Stars and Planetary Systems*, ed. CJ Lada, ND Kylafis, pp. 143–92. Dordrecht: Kluwer

Lahuis F, van Dishoeck EF. 2000. *Astron. Astrophys.* 355:699–712

Larsson B, Liseau R, Men'shchikov AB. 2002. *Astron. Astrophys.* 386:1055–73

Le Bourlot J, Pineau des Forêts G, Flower DR, Cabrit S. 2002. *MNRAS* 332:985–93

Lefloch B, Cernicharo J, Cabrit S, Noriega-Crespo A, Moro-Martín, Cesarsky D. 2003. *Ap. J.* 590:L41–44

Lefloch B, Cernicharo J, Rodríguez LF, Miville-Deschênes MA, Cesarsky D, Heras AM. 2002. *Ap. J.* 581:335–56

Léger A, Puget JL. 1984. *Astron. Astrophys.* 137:L5–8

Lemke D, Klaas U, Abollins J, Ábrahám P, Acosta-Pulido J, et al. 1996. *Astron. Astrophys.* 315:L64–70

Li A, Draine BT. 2002. *Ap. J.* 572:232–37

Li W, Evans NJ, Jaffe DT, van Dishoeck EF, Thi WF. 2002. *Ap. J.* 568:242–58

Lis DC, Keene J, Phillips TG, Schilke P, Werner MW, Zmuidzinas J. 2001. *Ap. J.* 561:823–29

Liseau R, Ceccarelli C, Larsson B, Nisini B, White GJ, et al. 1996. *Astron. Astrophys.* 315:L181–84

Liseau R, Giannini T, Nisini B, Saraceno P, Spinoglio L, et al. 1997. See Reipurth & Bertout 1997, pp. 111–20

Liseau R, White GJ, Larsson B, Sidher S, Olofsson G, et al. 1999. *Astron. Astrophys.* 344:342–54

Lorenzetti D, Giannini T, Nisini B, Benedettini M, Creech-Eakman M, et al. 2000. *Astron. Astrophys.* 357:1035–44

Lorenzetti D, Giannini T, Nisini B, Benedettini M, Elia D, et al. 2002. *Astron. Astrophys.* 395:637–45

Lorenzetti D, Tommasi E, Giannini T, Nisini B, Benedettini M, et al. 1999. *Astron. Astrophys.* 346:604–16

Malfait K, Waelkens C, Bouwman J, de Koter A, Waters LBFM. 1999. *Astron. Astrophys.* 345:181–86

Malfait K, Waelkens C, Waters LBFM, Vandenbussche B, Huygen E, de Graauw MS. 1998. *Astron. Astrophys.* 332:L25–28

Maret S, Ceccarelli C, Caux E, Tielens AGGM, Castets A. 2002. *Astron. Astrophys.* 395:573–85

Mattila K, Lemke D, Haikala LK, Laureijs RJ, Léger A, et al. 1996. *Astron. Astrophys.* 315:L353–56

Meeus G, Bouwman J, Dominik C, Waters LBFM, de Koter A. 2002. *Astron. Astrophys.* 392:1039–46

Meeus G, Waters LBFM, Bouwman J, van den Ancker ME, Waelkens C, Malfait K. 2001. *Astron. Astrophys.* 365:476–90

Melnick G, Gull GE, Harwit M. 1979. *Ap. J. Lett.* 227:L29–33

Mennella V, Muñoz-Caro GM, Ruiterkamp R, Schutte WA, Greenberg JM, et al. 2001. *Astron. Astrophys.* 367:355–61

Minh YC, van Dishoeck EF, eds. 2000. *IAU Symp. 197, Astrochem.* San Francisco: ASP. 597 pp.

Miroshnichenko A, Ivezic Z, Vinkovic D, Elitzur M. 1999. *Ap. J.* 520:L115–18

Molinari S, Ceccarelli C, White GJ, Saraceno P, Nisini B, et al. 1999. *Ap. J.* 521:L71–74

Molinari S, Noriega-Crespo A. 2002. *Astron. J.* 123:2010–18

Molinari S, Noriega-Crespo A, Ceccarelli C, Nisini B, Giannini T, et al. 2000. *Ap. J.* 538:698–709

Molinari S, Noriega-Crespo A, Spinoglio L. 2001. *Ap. J.* 547:292–301

Molster FJ, Waters LBFM. 2003. See Henning 2003, pp. 121–70

Molster FJ, Waters LBFM, Tielens AGGM, Koike C, Chihara H. 2002. *Astron. Astrophys.* 382:241–55

Moneti A, Cernicharo J. 2000. See Salama et al. 2000, pp. 119–22

Moore MH, Hudson RL. 1998. *Icarus* 135:518–27

Moos HW, Sembach KR, Vidal–Madjar A, York DG, Friedman SD, et al. 2002. *Ap. J. Suppl.* 140:3–17

Moro-Martín A, Noriega-Crespo A, Molinari S, Testi L, Cernicharo J, Sargent A. 2001. *Ap. J.* 155:146–59

Moutou C, Sellgren K, Verstraete L, Léger A. 1999a. *Astron. Astrophys.* 347:949–56

Moutou C, Verstraete L, Léger A, Sellgren K, Schmidt W. 2000. *Astron. Astrophys.* 354:L17–20

Moutou C, Verstraete L, Sellgren K, Léger A. 1999b. See Cox & Kessler 1999, pp. 727–30

Najita J, Carr JS, Mathieu RD. 2003. *Ap. J.* 589:931–52

Natta A, Meyer MR, Beckwith SVW. 2000. *Ap. J.* 534:838–45

Natta A, Prusti T, Neri R, Wooden D, Grinin VP, Mannings V. 2001. *Astron. Astrophys.* 371:186–97

Neufeld DA, Melnick GJ, Harwit M. 1998. *Ap. J.* 506:L75–78

Neufeld DA, Zmuidzinas J, Schilke P, Phillips TG. 1997. *Ap. J.* 488:L141–44

Nisini B, Benedettini M, Giannini T, Caux E, Di Giorgio AM, et al. 1999a. *Astron. Astrophys.* 350:529–40

Nisini B, Benedettini M, Giannini T, Clegg PE, Di Giorgio AM, et al. 1999b. *Astron. Astrophys.* 343:266–72

Nisini B, Benedettini M, Giannini T, Codella C, Lorenzetti D, et al. 2000. *Astron. Astrophys.* 360:297–310

Nisini B, Giannini T, Lorenzetti D. 2002. *Ap. J.* 574:246–57

Nisini B, Lorenzetti D, Cohen M, Ceccarelli C, Giannini T, et al. 1996. *Astron. Astrophys.* 315:L321–24

Noriega-Crespo A. 2002. *Rev. Mex. Astron. Astrofis.* 13:71–78

Nummelin A, Whittet DCB, Gibb EL, Gerakines PA, Chiar JE. 2001. *Ap. J.* 558:185–93

Okada Y, Onaka T, Shibai H, Doi Y. 2003. *Astron. Astrophys.* 412:199–212

Omont A, Gilmore GF, Alard C, Aracil B, August T, et al. 2003. *Astron. Astrophys.* 403:975–92

Onaka T, Okada Y. 2003. *Ap. J.* 585:872–77

Onaka T, Yamamura I, Tanabe T, Roellig TL, Yuen L. 1996. *Publ. Astron. Soc. Jpn.* 48:L59–63

Parmar PS, Lacy JH, Achtermann JM. 1991. *Ap. J. Lett.* 372:L25–28

Peeters E, Allamandola LJ, Bauschlicher CW, Hudgins DM, Sandford SA, Tielens AGGM. 2004a. *Ap. J. Lett.* 604:252–57

Peeters E, Allamandola LJ, Hudgins DM, Hony S, Tielens AGGM. 2004b. In *The Astrophysics of Dust*, ed. AN Witt, GC Clayton, BT Draine. San Francisco: ASP. In press

Peeters E, Hony S, van Kerckhoven C, Tielens AGGM, Allamandola LJ, et al. 2002a. *Astron. Astrophys.* 390:1089–113

Peeters E, Martín-Hernández NL, Damour F, Cox P, Roelfsema PR, et al. 2002b. *Astron. Astrophys.* 381:571–605

Pendleton YJ, Allamandola LJ. 2002. *Ap. J. Suppl.* 138:75–98

Pendleton YJ, Tielens AGGM, Tokunaga AT, Bernstein MP. 1999. *Ap. J.* 513:294–304

Poglitsch A, Hermann F, Genzel R, Madden SC, Nikola T, et al. 1996. *Ap. J. Lett.* 462:L43–46

Polehampton ET, Baluteau JP, Ceccarelli C, Swinyard BM, Caux E. 2002. *Astron. Astrophys.* 388:L44–47

Rho J, Reach W. 2003. *Rev. Mex. Astron. Astrofis.* 15:263–66

Reipurth B, Bertout C, eds. 1997. *Herbig-Haro Flows and the Birth of Stars*, IAU Symp. 182. Dordrecht: Kluwer. 596 pp.

Richter MJ, Jaffe DT, Blake GA, Lacy JH. 2002. *Ap. J. Lett.* 572:L161–64

Rietmeijer FJM, Hallenbeck SL, Nuth JA, Karner JM. 2002. *Icarus* 156:269–86

Rigopoulou D, Kunze D, Lutz D, Genzel R, Moorwoord AFM. 2002. *Astron. Astrophys.* 389:374:86

Rosenthal D, Bertoldi F, Drapatz S. 2000. *Astron. Astrophys.* 356:705–23

Salama A, Kessler MF, Leech K, Schulz B, eds. 2000. *2nd ISO Workshop Analyt. Spectrosc.*, ESA SP-456. Noordwijk: ESA-ESTEC. 389 pp.

Sandford SA, Bernstein MP, Allamandola LJ, Goorvitch D, Teixeira TCVS. 2001. *Ap. J.* 548:836–51

Saraceno P, Nisini B, Benedettini M, Di Giorgio AM, Giannini T, et al. 1999. See Cox & Kessler 1999, pp. 575–78

Schneider N, Simon R, Kramer C, Kraemer K, Stutzki J, Mookerjea B. 2003. *Astron. Astrophys.* 406:915–35

Schreyer K, Henning Th, van der Tak FFS, Boonman AMS, van Dishoeck EF. 2002. *Astron. Astrophys.* 394:561–83

Schutte WA. 1999. See d'Hendecourt et al. 1999, pp. 183–98

Schutte WA, Boogert ACA, Tielens AGGM, Whittet DCB, Gerakines PA, et al. 1999. *Astron. Astrophys.* 343:966–76

Schutte WA, Khanna RK. 2003. *Astron. Astrophys.* 398:1049–62

Schutte WA, Tielens AGGM, Whittet DCB, Boogert ACA, Ehrenfreund P, et al. 1996. *Astron. Astrophys.* 315:L333–36

Schutte WA, van der Hucht KA, Whittet DCB, Boogert ACA, Tielens AGGM, et al. 1998. *Astron. Astrophys.* 337:261–74

Sellgren K. 1984. *Ap. J.* 277:623–33

Sempere MJ, Cernicharo J, Lefloch B, González-Alfonso E, Leeks S. 2000. *Ap. J.* 530:L123–27

Siebenmorgen R, Prusti T, Natta A, Müller TG. 2000. *Astron. Astrophys.* 361:258–64

Smith MD, Froebrich D, Eislöffel J. 2003. *Ap. J.* 592:245–54

Smith RG, Sellgren K, Tokunaga AT. 1989. *Ap. J.* 344:413–26

Snell RL, Howe JE, Ashby MLN, Bergin EA, Chin G, et al. 2000. *Ap. J.* 539:L101–4

Snow TP, Rachford BL, Tumlinson J, Shull JM, Welty DE, et al. 2000. *Ap. J.* 538:L65–68

Spinoglio L, Giannini T, Nisini B, van den Ancker ME, Caux E, et al. 2000. *Astron. Astrophys.* 353:1055–64

Spitzer L, Cochran WD. 1973. *Ap. J. Lett.* 186:L23–28

Stacey GJ, Geis N, Genzel R, Lugten JB, Poglitsch A, et al. 1991. *Ap. J.* 373:423–44

Stantcheva T, Shematovich VI, Herbst E. 2002. *Astron. Astrophys.* 391:1069–80

Sternberg A, Dalgarno A. 1989. *Ap. J.* 338:197–233

Sternberg A, Neufeld DA. 1999. *Ap. J.* 516: 371–80

Taban IM, Schutte WA, Pontoppidan KM, van Dishoeck EF. 2003. *Astron. Astrophys.* 399:169–75

Teixeira TC, Devlin JP, Buch V, Emerson JP. 1999. *Astron. Astrophys.* 347:L19–22

Thi WF, Blake GA, van Dishoeck EF, van Zadelhoff GJ, Horn J, et al. 2001a. *Nature* 409:60–63

Thi WF, van Dishoeck EF, Black JH, Jansen DJ, Evans NJ, Jaffe DT. 1999. See Cox & Kessler 1999, pp. 767–70

Thi WF, van Dishoeck EF, Blake GA, van Zadelhoff GJ, Horn J, et al. 2001b. *Ap. J.* 561:1074–94

Tielens AGGM, Charnley SB. 1997. *Origin Life* 27:23–51

Tielens AGGM, Hagen W. 1982. *Astron. Astrophys.* 114:245–60

Tielens AGGM, Hollenbach DJ. 1985. *Ap. J.* 291:722–46

Tielens AGGM, Hony S, van Kerckhoven C, Peeters E. 2000. See Minh & van Dishoeck 2000, pp. 349–62

Tielens AGGM, Peeters E. 2004. In *The Dense Interstellar Medium in Galaxies*, ed. S Pfalzner, C Kramer, C Straubmeier, A Heithausen, pp. 497–506. Berlin: Springer-Verlag

Tielens AGGM, Tokunaga AT, Geballe TR, Baas F. 1991. *Ap. J.* 381:181–99

Timmermann R. 1998. *Ap. J.* 498:246–55

Timmermann R, Bertoldi F, Wright CM, Drapatz S, Draine BT, et al. 1996. *Astron. Astrophys.* 315:L281–84

Timmermann R, Köster B, Stutzki J. 1998. *Astron. Astrophys.* 336:L53–56

Valentijn EA, van der Werf PP. 1999. *Ap. J. Lett.* 522:L29–33

Valentijn EA, van der Werf PP, de Graauw Th, de Jong T. 1996, *Astron. Astrophys.* 315:L145–48

van Broekhuizen FA, Keane JV, Schutte WA. 2004. *Astron. Astrophys.* 415:425–36

van den Ancker ME. 2000. *Circumstellar material in young stellar objects*. PhD thesis, Univ. Amsterdam. 204 pp.

van den Ancker ME, Bouwman J, Wesselius PR, Waters LBFM, Dougherty SM, van Dishoeck EF. 2000a. *Astron. Astrophys.* 357:325–29

van den Ancker ME, Tielens AGGM, Wesselius PR. 2000b. *Astron. Astrophys.* 358:1035–48

van den Ancker ME, Wesselius PR, Tielens AGGM. 2000c. *Astron. Astrophys.* 355:194–210

van den Ancker ME, Wesselius PR, Tielens AGGM, van Dishoeck EF, Spinoglio L. 1999. *Astron. Astrophys.* 348:877–87

Vandenbussche B, Ehrenfreund P, Boogert ACA, van Dishoeck EF, Schutte WA, et al. 1999. *Astron. Astrophys.* 346:L57–60

van der Tak FFS, van Dishoeck EF, Caselli P. 2000a. *Ap. J.* 361:327–39

van der Tak FFS, van Dishoeck EF, Evans NJ, Blake GA. 2000b. *Ap. J.* 537:283–303

van Dishoeck EF. 1998. *Faraday Disc.* 109:31–46

van Dishoeck EF. 2003. In *Chemistry as a Diagnostic of Star Formation*, ed. CL Curry, M Fich, pp. 201–13. Ottawa: NRC

van Dishoeck EF, Black JH, Boogert ACA, Boonman AMS, Ehrenfreund P, et al. 1999. See Cox & Kessler 1999, pp. 437–48

van Dishoeck EF, Helmich FP. 1996. *Astron. Astrophys.* 315:L177–80

van Dishoeck EF, Helmich FP, de Graauw Th, Black JH, Boogert ACA, et al. 1996. *Astron. Astrophys.* 315:L349–52

van Dishoeck EF, Tielens AGGM. 2001. In *The Century of Space Science*, ed. JAM Bleeker, J Geiss, MCE Huber, pp. 607–45. Dordrecht: Kluwer

van Dishoeck EF, Wright CM, Cernicharo J, González-Alfonso E, Helmich FP, et al. 1998. *Ap. J. Lett.* 502:L173–76

van Kerckhoven C, Hony S, Peeters E, Tielens AGGM, Allamandola LJ, et al. 2000. *Astron. Astrophys.* 357:1013–19

Vastel C, Caux E, Ceccarelli C, Castets A, Gry C, Baluteau JP. 2000. *Astron. Astrophys.* 357:994–1000

Vastel C, Polehampton ET, Baluteau JP, Swinyard BM, Caux E, Cox P. 2002. *Ap. J.* 581:315–24

Vastel C, Spaans M, Ceccarelli C, Tielens AGGM, Caux E. 2001. *Astron. Astrophys.* 376:1064–72

Verstraete L, Pech C, Moutou C, Sellgren K, Wright CM, et al. 2001. *Astron. Astrophys.* 372:981–97

Verstraete L, Puget JL, Falgarone E, Drapatz S, Wright CM, Timmermann R. 1996. *Astron. Astrophys.* 315:L337–40

Waelkens C, Waters LBFM, de Graauw Th, Huygen E, Malfait K, et al. 1996. *Astron. Astrophys.* 315:L245–48

Walmsley CM, Pineau des Forêts G, Flower DR. 1999. *Astron. Astrophys.* 342:542–50

Ward-Thompson D, André P, Kirk JM. 2002. *MNRAS* 329:257–76

Waters LBFM, Waelkens C. 1998. *Annu. Rev. Astron. Astrophys.* 36:233–66

Waters LBFM, Waelkens C, van der Hucht KA, Zaal PA, eds. 1998. *ISO's View on Stellar Evolution*. Dordrecht: Kluwer. 530 pp.

White GJ, Liseau R, Men'shchikov AB, Justtanont K, Nisini B, et al. 2000. *Astron. Astrophys.* 364:741–62

Willner SP, Gillett FC, Herter TL, Jones B, Krassner J, et al. 1982. *Ap. J.* 253:174–87

Wright CM. 2000. See Minh & van Dishoeck 2000, pp. 177–90

Wright CM, Drapatz S, Timmermann R, van der Werf PP, Katterloher R, de Graauw Th. 1996. *Astron. Astrophys.* 315:L301–4

Wright CM, Timmermann R, Drapatz S. 1997. See Heras et al. 1997, pp. 311–12

Wright CM, van Dishoeck EF, Black JH, Feuchtgruber J, Cernicharo J, et al. 2000. *Astron. Astrophys.* 358:689–700

Wright CM, van Dishoeck EF, Cox P, Sidher SD, Kessler MF. 1999. *Ap. J. Lett.* 515:L29–33

Yun J, Liseau R, eds. 1998. *Star Formation with the Infrared Space Observatory*, Vol. 132. San Francisco: ASP. 448 pp.

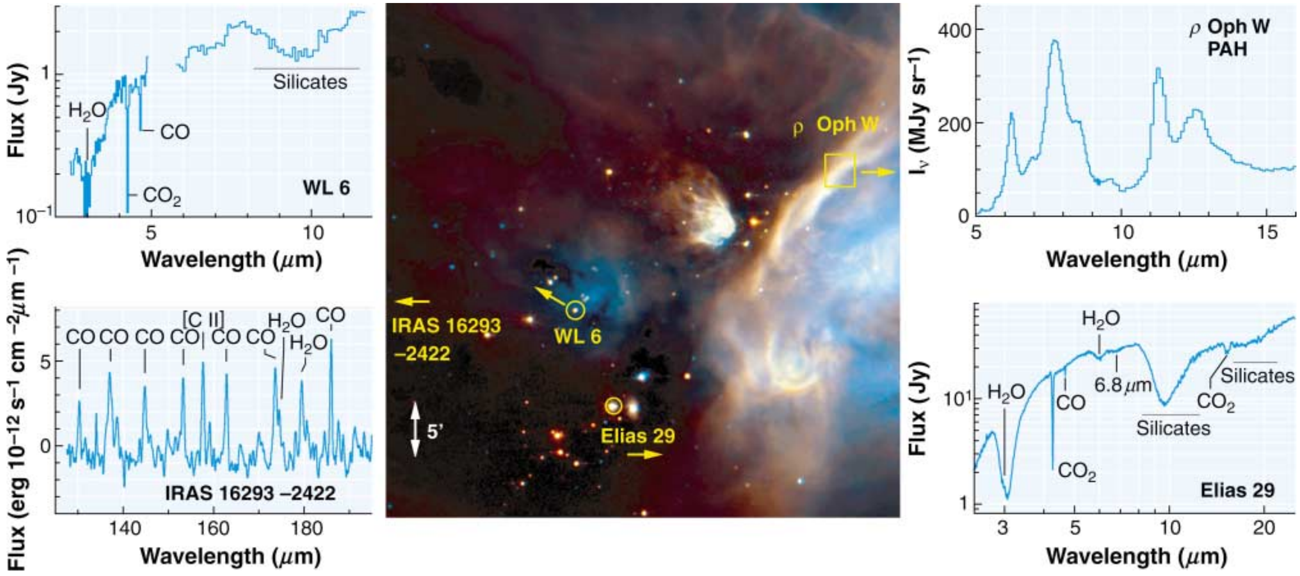

Figure 1 ISOCAM composite 7 and 15 μm image of the ρ Oph molecular cloud. The bright filaments in the west trace the hot dust illuminated by the B2V star HD 147889 located just outside the map. The dense cloud containing *IRAS* 16293-2422 is to the east. The dark patches are very dense cores that are optically thick even at 15 μm, whereas the bright point sources throughout the image are mostly low-mass YSOs. The majority of the extended 7μm emission is due to PAHs (Abergel et al. 1996). Spectra of various objects in ρ Oph are indicated on the side. PHOT-S spectrum of WL 6 (*left top*) (J. Gürtler, unpublished data), CAM-CVF spectrum of ρ Oph W (*right top*) (Boulanger et al. 2000), LWS spectrum of *IRAS* 16293-2422 (*left bottom*) (Ceccarelli et al. 1998a), SWS spectrum of Elias 29 (*right bottom*) (Boogert et al. 2000b).

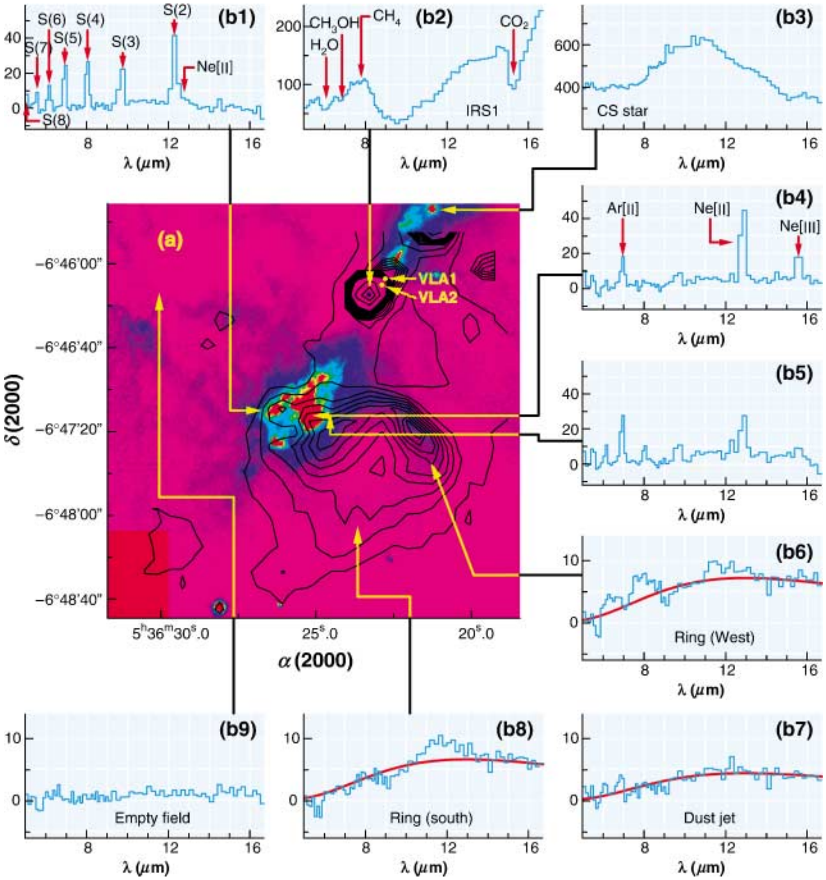

Figure 2 CAM-CVF image of the HH 1–2 region by Cernicharo et al. (2000b), illustrating a wide variety of types of spectra, ranging from ice absorptions toward the class 0 protostar VLA1 (spectrum b2) to silicate emission from a disk around the Cohen-Schwarz star (spectrum b3) and gas emission from shocks (spectra b1, b4, b5). Both low-velocity shocks (v ≈ 10–15) km s^{-1} as traced by the strong H_2 lines in panel b1 and high-velocity shocks (v ≈ 100–140 km s^{-1}), as traced by the [Ne II] and [Ne III] lines in panel b4 are seen. Note the complete absence of any continuum emission owing to hot dust and PAH emission in both panels. The color image is a [Si II] 6717 Å optical image, whereas the black contours indicate the 7 μm CAM image. The intensity scale is in mJy.

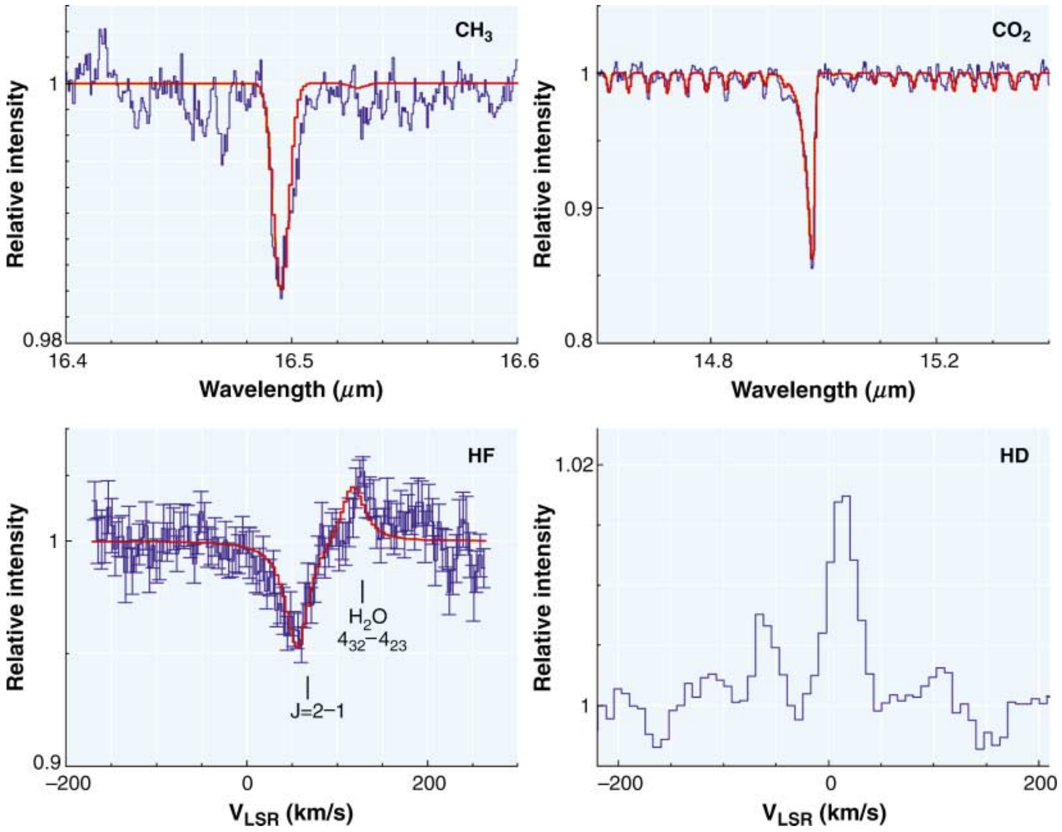

Figure 5 New gas-phase molecules detected by *ISO*. The red line in each panel indicates the model spectrum. CH$_3$ ν_2 Q-branch toward Sgr A* (*top left*) (Feuchtgruber et al. 2000); CO$_2$ ν_2 band toward AGFL 2136 (*top right*) (van Dishoeck et al. 1996, Boonman et al. 2003b); HF $J = 2 - 1$ toward Sgr B2 (*bottom left*) (Neufeld et al. 1997); HD $J = 1 - 0$ line toward the Orion Bar (*bottom right*) (Wright et al. 1999).

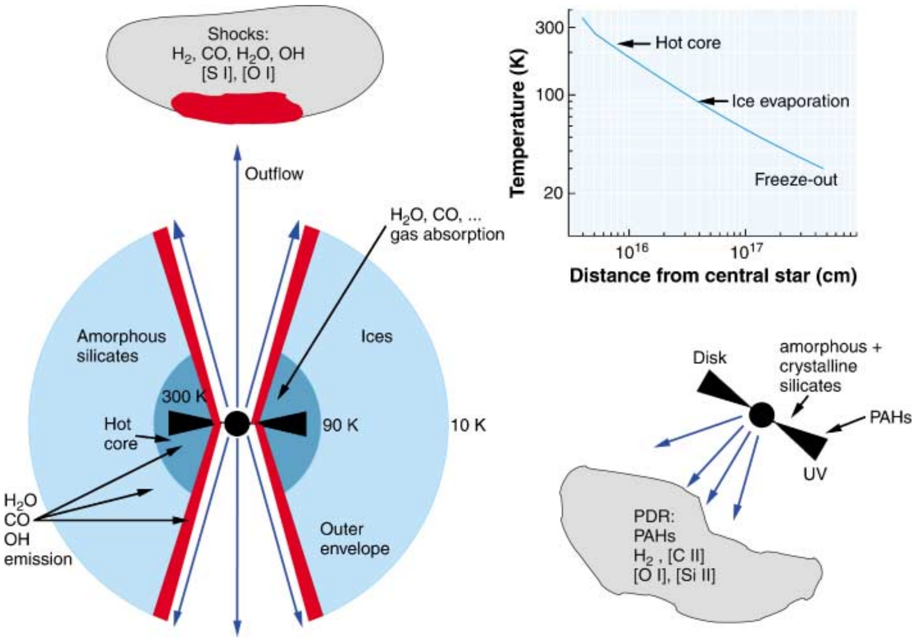

Figure 6 Cartoon of the environment of young stellar objects and the origin of the various spectral features observed by *ISO*. The top diagram indicates the typical temperature structure of a protostellar envelope, with the critical temperatures for freeze-out, ice evaporation, and high-temperature chemistry indicated.

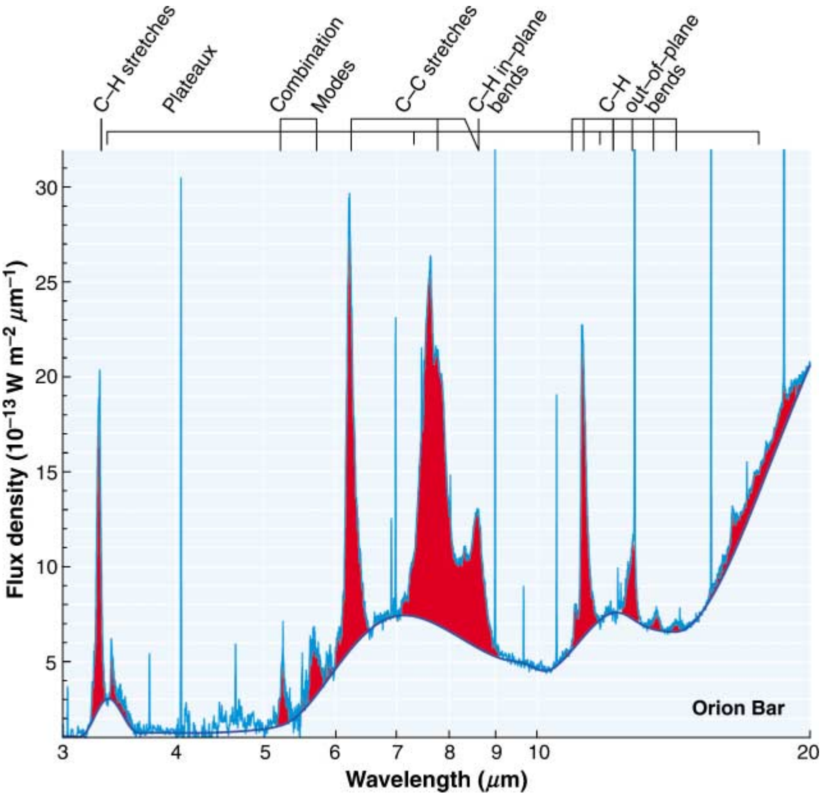

Figure 8 SWS spectrum of the Orion Bar PDR, illustrating the richness of PAH features. Various atomic and molecular lines are seen as well, originating in the PDR and in the Orion H II region along the line of sight. The spectrum is taken at the position of the peak of the H_2 $v = 1 - 0$ S(1) emission (Peeters et al. 2004b).

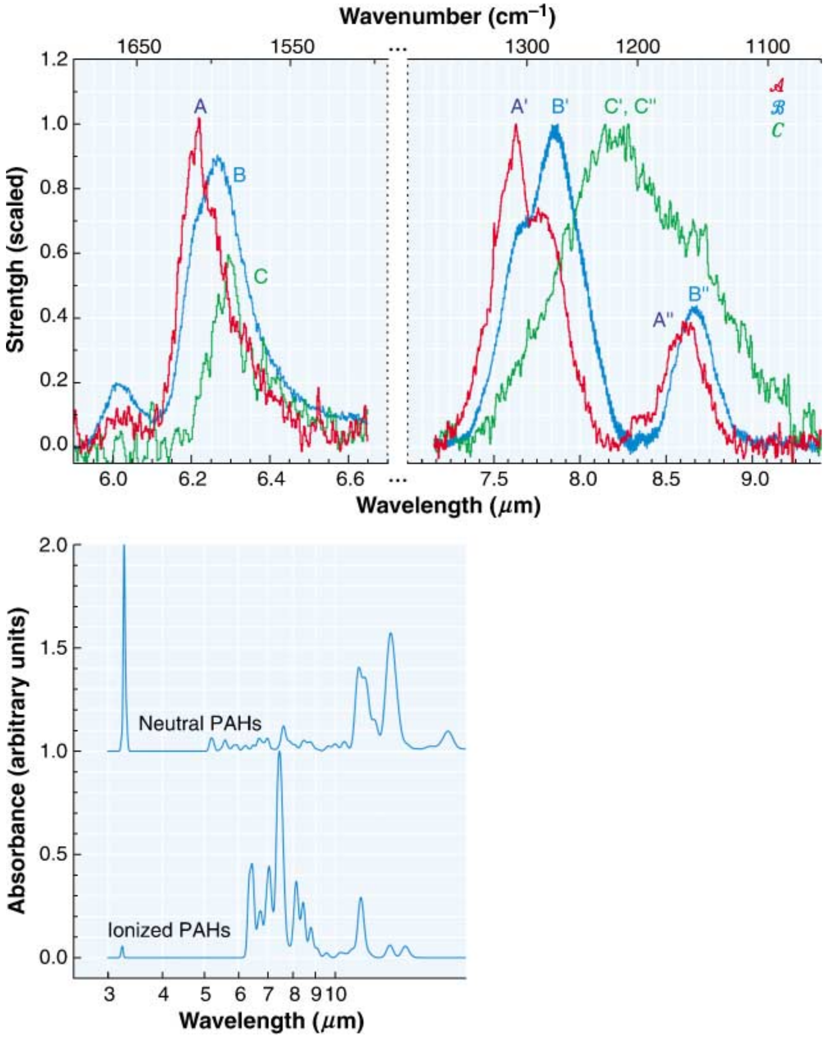

Figure 9 (*Top*) Source to source variations observed for the 6–9 μm PAH features with the SWS. Profile A is representative of all PDRs and reflection nebulae, including the diffuse interstellar medium. Profile B refers to the isolated Herbig Ae stars with disks, as well as most planetary nebulae. Profile C is observed for some post-AGB objects (Peeters et al. 2002a). (*Bottom*) Laboratory spectra of a mixture of neutral PAHs compared with that of positively ionized PAHs. Note the stronger 3.3 μm feature for neutral PAHs and the stronger 6–9 μm complex for ionized PAHs (figure adapted from Allamandola et al. 1999).

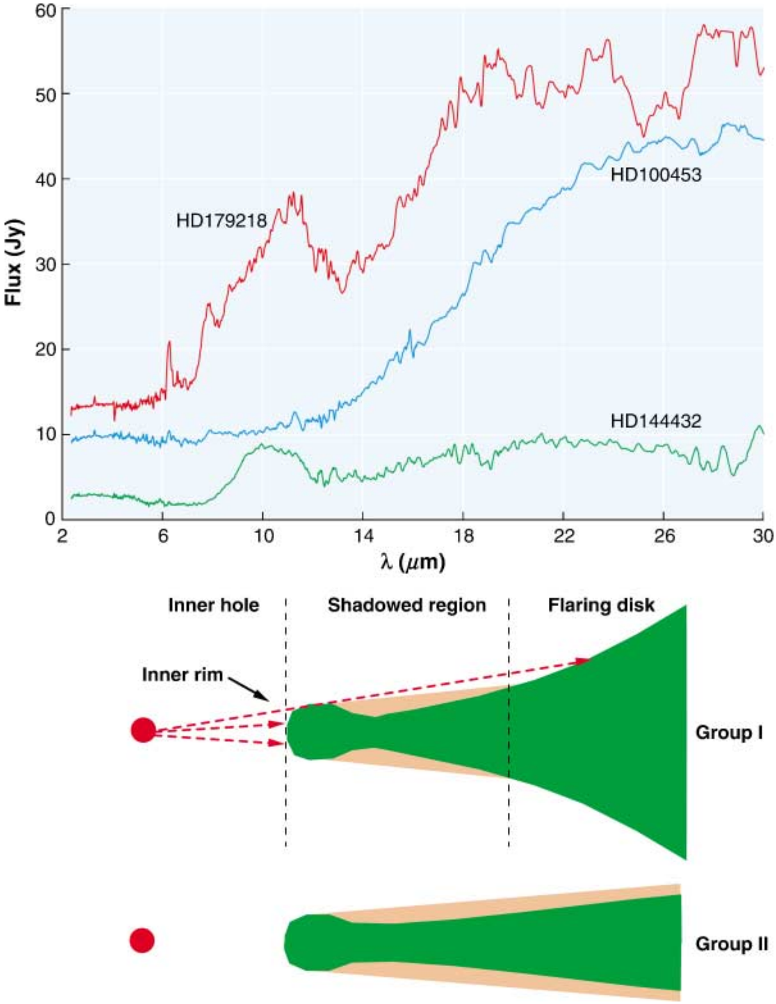

Figure 10 (*Top*) SWS spectra of disks around isolated Herbig Ae stars, illustrating their different spectral characteristics. HD 179218 is an example of a source with crystalline silicates, whereas HD 100453 does not show any 10 μm emission. Both sources have rising SEDs (Group I). HD 144432 is an example of a source with a flat SED (Group II). The HD 144432 and HD 100453 spectra have been shifted by –5 and –10 Jy for clarity. (*Bottom*) Sketch of the different geometries for Group I and II sources. The silicate emission is thought to arise from the warm upper layers in the inner disk, whereas the PAH emission can also come from the flaring outer part (Meeus et al. 2001, Dullemond & Dominik 2004).

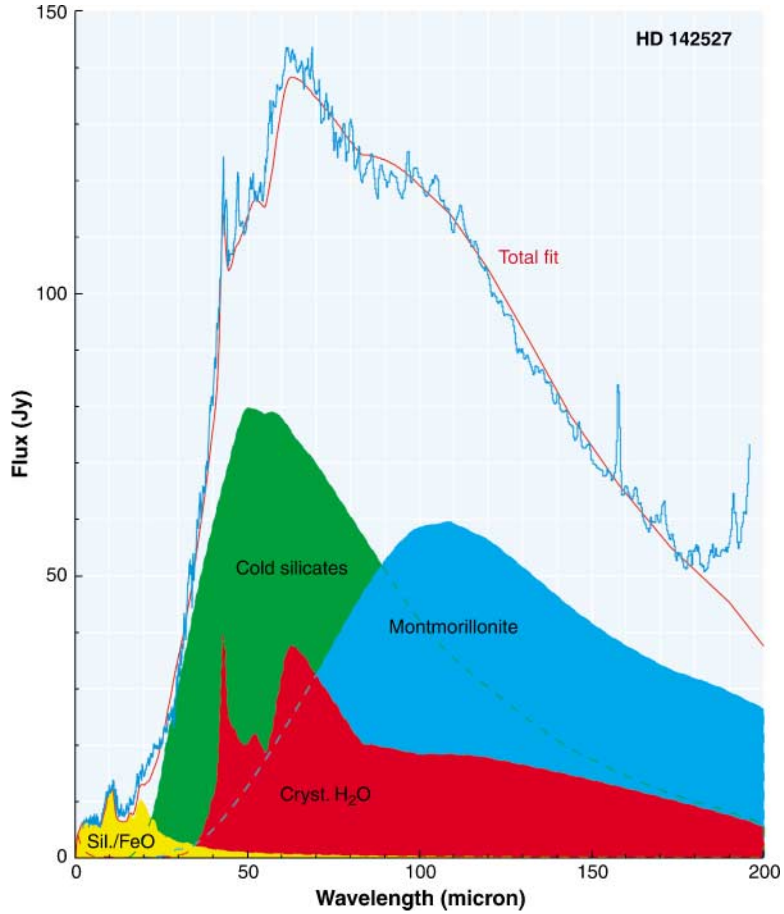

Figure 11 Complete SWS-LWS spectrum of the isolated Herbig Ae star HD 142527, together with the decomposition into the different components, including hot and cold amorphous silicates, crystalline H_2O ice, and tentatively the crystalline hydrous silicate montmorillonite (Malfait et al. 1999).

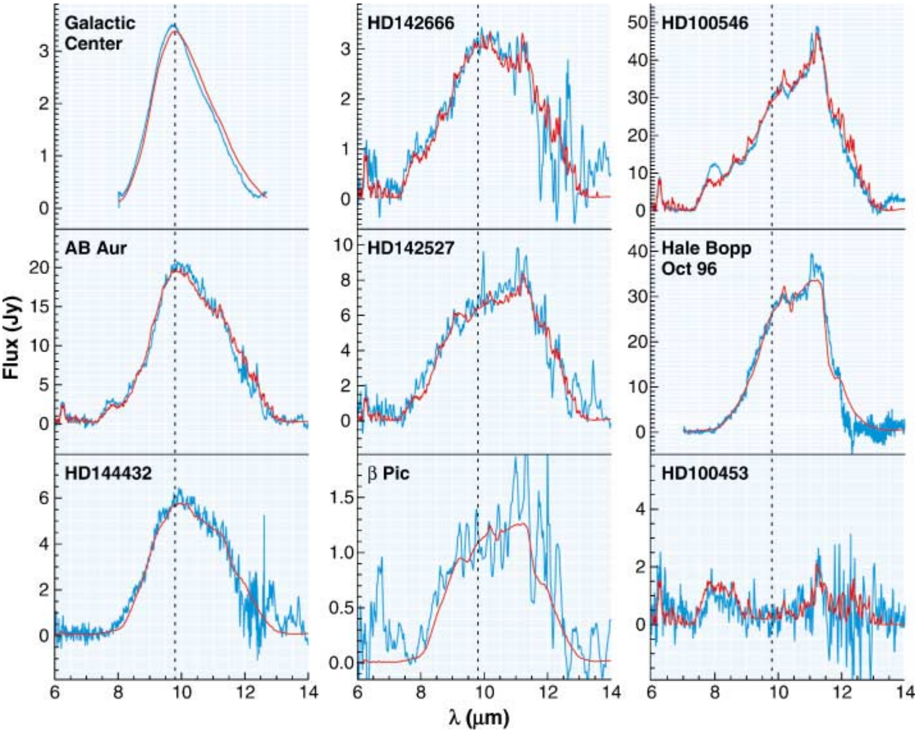

Figure 12 Continuum-subtracted 10 μm silicate emission bands observed toward a selected sample of isolated Herbig Ae stars with the SWS. For reference, the silicate bands of interstellar medium dust and comet C/1995 O1 Hale-Bopp are included. The dashed line indicates the position of the 9.8 μm amorphous silicate band observed in the interstellar medium. The full lines indicate the best-fit models using a mixture of amorphous and crystalline material with different grain sizes. The sharp 11.3 μm feature is evidence for crystallization: the shift toward longer wavelengths for grain growth (Bouwman et al. 2001).

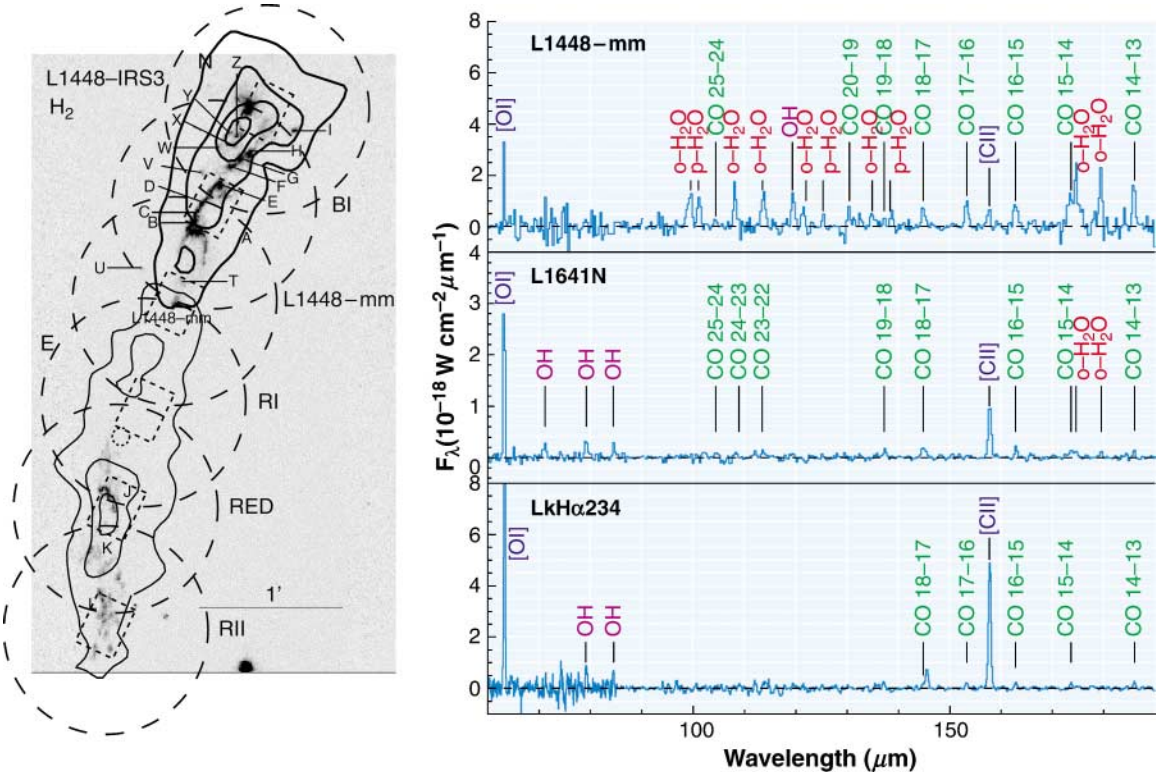

Figure 14 (*Left*) narrow-band image of the L1448 outflow at 2.12 μm (H_2 + continuum), with superposed the LWS (*long dashed circles*) and SWS (*short dashed rectangles*) apertures. The thick and thin solid lines delineate the contours of the blue- and red-shifted CO outflow from the L1448-mm source (Nisini et al. 2000). (*Right*) LWS continuum-subtracted spectrum toward the Class 0 source L1448-mm compared with the more evolved L1641N and LkHα 234 sources. Note the decrease of molecular emission, in particular H_2O, toward the latter sources (Benedettini et al. 2003).

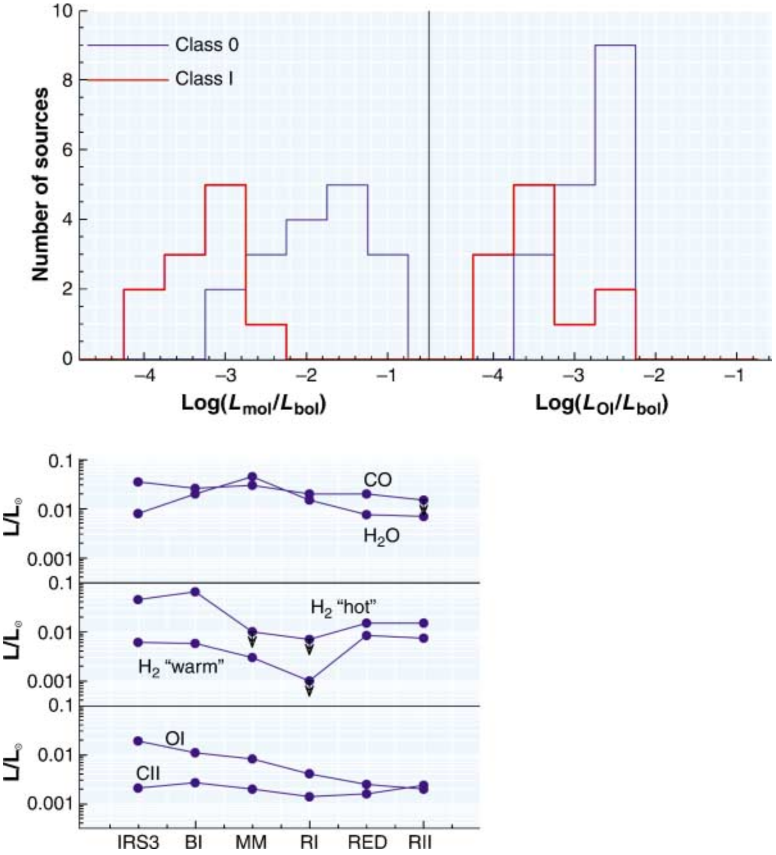

Figure 15 (*Top*) histogram of the total molecular cooling, defined as $L_{\mathrm{mol}} = L_{\mathrm{H_2O}} + L_{\mathrm{CO}} + L_{\mathrm{OH}}$, and of the cooling owing to [O I], compared with the source bolometric luminosity for a set of embedded YSOs (Nisini et al. 2002). (*Bottom*) Luminosity emitted by different molecular and atomic species along the L1448 outflow (see Figure 14 for positions). Warm and hot H_2 refer to the pure rotational and vibration-rotation lines, respectively (Nisini et al. 2000).

AR Annual Review of Astronomy and Astrophysics
Volume 42, 2004

CONTENTS

INDEXES

ERRATA

An online log of corrections to *Annual Review of Astronomy and Astrophysics* chapters may be found at http://astro.annualreviews.org/errata.shtml